Rates of Evacuation of Bedload Sediment From an Alpine Glacier Control Proglacial Stream Morphodynamics

D. Mancini[1] , M. Roncoroni[2] , M. Dietze[3,4] , M. Jenkin[1] , T. Müller[1] , B. Ouvry[5], F. Miesen[1] , Q. Pythoud[1], M. Hofmann[1], F. Lardet[1], A. P. Nicholas[6], and S. N. Lane[1]

[1]Institute of Earth Surface Dynamics (IDYST), Université de Lausanne, Lausanne, Switzerland, [2]Institut National de la Recherche Scientifique (INRS), Québec City, QC, Canada, [3]Intitute of Geography, Georg-August-University Göttingen, Göttingen, Germany, [4]German Research Center for Geosciences (GFZ), Potsdam, Germany, [5]Glaciology and Geomorphodynamics, Department of Glaciology, University of Zürich, Zürich, Switzerland, [6]Geography, Faculty of Environment, Science and Economy, University of Exeter, Exeter, UK

Abstract Proglacial forefields commonly include highly dynamic fluvial systems associated with the fundamental instability between topography, flow hydraulics and sediment transport. However, there is limited knowledge of how these systems respond to changing subglacial hydrology and sediment supply. We investigated this relationship using the first continuous field-collected data sets for both suspended and bedload sediment export and proglacial river dynamics for an Alpine glacier forefield, the Glacier d'Otemma, Switzerland. The results show a strong sensitivity of fluvial morphodynamics to the balance between sediment transport capacity and supply. When subglacial bedload export rates exceeded fluvial transport capacity, we found bar construction leading to net forefield aggradation and surficial coarsening, especially on bar heads. This intensified braiding buffered the downstream transport of coarse sediment. When subglacial bedload export rates were lower than transport capacity, incision occurred, with reduced braiding intensity, net erosion and important amounts of bedload leaving the proglacial system. We found a net fining of surficial deposits except for very isolated coarsening patterns on bar heads. Thus, proglacial forefield morphodynamics are strongly conditioned by subglacial hydrology and sediment supply, but this conditioning is also influenced by the response of the forefield itself. Proglacial forefields have an important influence on the longitudinal connectivity of sediment flux in regions sensitive to climate change, such as recently deglaciated high mountain areas. The linkages we report between subglacial processes and river morphodynamics are critical for understanding the development of embryonic forefield ecosystems.

Plain Language Summary This study focuses on Alpine proglacial forefields, braided fluvial streams flowing in deglaciated terrains, and their geomorphic response to both sediment and water exported from retreating glaciers. This is achieved using the first continuous field-collected data sets combining sediment flux quantifications at the glacier terminus and downstream changes of the river over time collected in the Glacier d'Otemma forefield (Switzerland). Results show that the fluvial landscape in recently deglaciated terrains changes rapidly, influenced by the balance between the amount of sediment being transported from under the glacier and the river's capacity to carry it. When the released amount of sediment matches the river's capacity, the deposition of coarser material dominates and the stream becomes more complex with increasing braiding intensity. However, when the river carries more sediment than supplied by the glacier, flow becomes more confined into fewer channels, promoting the erosion of previously deposited material, particularly for the coarser sediment fractions. The study emphasizes how both the river configuration and the landscape near a melting glacier depend on whether the river itself can transport the quantities of sediment delivered by the glacier. This balance can affect the downstream sediment flux from glaciered catchments and the development of ecosystems following climate change-induced glacier retreat.

1. Introduction

Proglacial margins are increasing in size following rapid glacier retreat. In the Swiss and Austrian Alps alone, ca. 930 km^2 of deglaciated terrain has been created since the end of the Little Ice Age (Carrivick et al., 2018). If there is lateral accommodation space and the valley slope is not sufficient to allow the river to evacuate all the sediment supplied to it, active, fluvially reworked forefields may develop in the proglacial margin. Such systems are thought to be amongst the most dynamic and active landscapes on Earth because of their sensitivity to varying

Project administration: S. N. Lane
Resources: D. Mancini, M. Roncoroni, M. Jenkin, T. Müller, B. Ouvry, F. Miesen, Q. Pythoud, M. Hofmann, F. Lardet, S. N. Lane
Software: D. Mancini, M. Dietze
Supervision: A. P. Nicholas, S. N. Lane
Validation: D. Mancini
Writing – original draft: D. Mancini
Writing – review & editing: D. Mancini, M. Roncoroni, M. Dietze, M. Jenkin, T. Müller, B. Ouvry, F. Miesen, Q. Pythoud, M. Hofmann, F. Lardet, A. P. Nicholas, S. N. Lane

discharge and sediment supply in both space and time (Ashmore, 1988, 1991a; Lane et al., 1996), conditions which themselves have become more intense since deglaciation (Huss & Hock, 2018; Lane et al., 2017; Lane & Nienow, 2019; Zhang et al., 2023).

Braided stream mechanisms for both sand- and gravel-systems have traditionally been studied in relatively small-scale field settings (e.g., Ashworth & Ferguson, 1989; Lane et al., 1996; Brasington et al., 2000; Williams et al., 2011), scaled laboratory experiments (e.g., Ashmore, 1982, 1991a,b; Ferguson & Ashworth, 1992; Germanoski & Schumm, 1993) and numerical simulations (e.g., Nicholas, 2013; Schuurman & Kleinhans, 2015; Williams et al., 2016). Such research has resulted in a good understanding of braiding processes, but less attention has been given to how they respond to subglacial processes (Carrivick & Heckmann, 2017). Subglacial discharge (Gimbert et al., 2016; Lane & Nienow, 2019; Riihimaki et al., 2005) and sediment supply (Lane et al., 2017; Perolo et al., 2019) both evolve systematically during the melt season of Alpine glaciers. The forefield river response is likely to be a function of the ratio of glacier-driven sediment supply to meltwater-driven transport capacity, both at the daily to weekly scale and also over longer timescales (Collins, 2008; Lane et al., 1996). Incision has been observed immediately in front of glaciers where a commonly single-thread subglacial stream enters the proglacial forefield and capacity exceeds supply, providing the sediment that may cause supply to exceed capacity further downstream and hence aggradation (Beylich et al., 2009; Germanoski & Schumm, 1993; Marren, 2002; Roussel et al., 2018). As glaciers retreat, the hinge point between upstream erosion and downstream deposition is thought to migrate upstream (Marren, 2002; Marren & Toomath, 2013, 2014). If supply can match or exceed capacity, aggradation may be present the whole forefield along with highly braided stream networks (Curran et al., 2017).

Whilst the temporal and spatial variability in sediment transport in these environments is driven by external forcing, it is also impacted by autogenic reorganization of the proglacial river itself (Coulthard et al., 2005; Coulthard & Van De Wiel, 2007; Marren & Toomath, 2014) notably with the progressive reworking of riverbed deposits (e.g., Ashmore, 1991b; Cudden & Hoey, 2003; Ferguson & Ashworth, 1992; Kasprak et al., 2015). It impacts particle advection lengths and attenuates the downstream transport of sediment (Ganti et al., 2014; Mancini et al., 2023b). In proglacial environments, the transport signal evolves with distance from being a function of subglacial sediment evacuation rates to being a function of reworking of the forefield itself (Jerolmack & Paola, 2010). Mancini et al. (2023b) tested this hypothesis for both suspended sediment and bedload flux using continuous records collected in an active proglacial forefield. They found strong filtering (i.e., dampening and delaying) of the subglacial sediment export signal for bedload but not suspended sediment whose signal passed almost unimpeded through the forefield. Proglacial forefield morphodynamics thus modify the longitudinal connectivity of sediment flux between glacier margins and downstream geomorphic systems.

Evidence suggests that proglacial forefields filter the signal of bedload exported from glaciers, but the interaction between braided stream morphology, sediment fluxes and topographical constraints is only partially understood (Ashmore et al., 2011; Davies, 1987; Maizels, 2002; Warburton, 1996). This is because measuring bedload transport continuously over long time periods (e.g., a glacial melt season) and quantifying the space-time dynamics of the proglacial river are both difficult. The development of passive environmental seismology for continuous bedload monitoring makes it possible to obtain continuous season-scale bedload transport data (e.g., Burtin et al., 2011; Dietze, 2018; Dietze et al., 2019; Mancini et al., 2023b). Developments in remote sensing, notably combining low-cost Uncrewed Airborne Vehicle (UAV) platforms combined with SfM (Structure-from-Motion)-MVS (Multi-View-Stereo) photogrammetry software to create Digital Elevation Models (DEMs), are allowing high-frequency quantification of morphodynamic changes (e.g., Fonstad et al., 2013). This paper harnesses both of these developments.

Given the relatively small influence of proglacial filtering on the suspended sediment signal (Mancini et al., 2023b), we hypothesize (a) that subglacial bedload export drives both geomorphic and morphodynamic responses of the proglacial stream which, in turn, control the downstream bedload flux. Following Collins (2008), a higher ratio between upstream bedload supply and transport capacity promotes aggradation as the stream evolves toward a more braided configuration. This results (b) in decreasing supply rates to downstream as the increasing presence of flow divergence regions buffers the downstream transport of coarser particles, which may also be detected in surface coarsening (Antoniazza et al., 2019; Ashmore, 1988; Kasprak et al., 2015; Mosley, 1983). In contrast, when capacity exceeds supply, we hypothesis (c) that net loss of bedload sediment causes the proglacial stream to evolve toward a less complex configuration (Germanoski & Schumm, 1993). We test
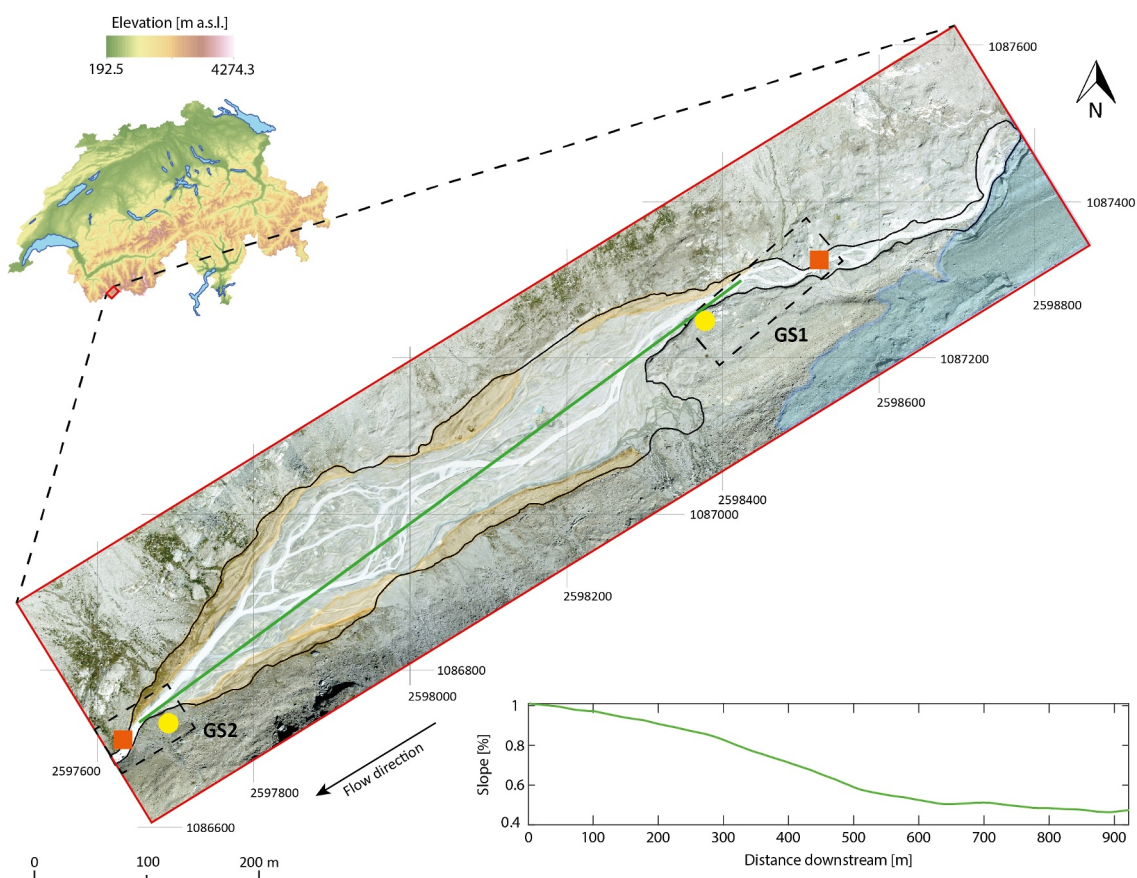
Figure 1. Location of the Glacier d'Otemma proglacial forefield and spatial location of monitoring stations GS1 and GS2. Orange squares refer to turbidity and water pressure sensors, while yellow dots highlight geophones. The solid black line refers to the limit of the proglacial forefield, while the dashed line refers to the extent of the monitoring stations. The shaded orange polygons show the terrace systems, while the light blue one shows the glacier. The green line highlights the downstream slope transect. Coordinates are in the Swiss CH1903+/LV95 geographic coordinate system. Source of the orthomosaic: Swisstopo (2020).

these hypotheses for an Alpine proglacial margin in front of the Glacier d'Otemma in south–west Switzerland for two entire melt seasons (2020 and 2021).

2. Methodology and Methods

2.1. Study Area

The forefield of the Glacier d'Otemma (southern–western Swiss Alps) is located at 2,450 m a.s.l. and is ca. 1 km long by ca. 200 m wide, including an active braided stream network (Figure 1). Upstream and downstream of the forefield, flow is confined into a single channel due to the combination of narrower valley sections and a steeper valley slope, the latter leading to a bedrock-dominated riverbed. A decadal-scale analysis of the evolution of its valley sidewall systems following glacial debuttressing confirmed that sidewall sediment supply is decoupled from the active forefield (Mancini & Lane, 2020). As already highlighted in other studies in the same region (i.e., Müller et al., 2024; Roncoroni et al., 2023b), other potential source of sediment and water could be considered geomorphologically and hydrologically negligible in this study.

The mean channel width of the straight section is ca. 10 m at the forefield inlet and ca. 8 m at the forefield outlet. Within the forefield, the longitudinal slope is between ca. 1% in the upper and ca. 0.45% in the lower section. The riverbed is dominated by a mixture of gravel and sand. The in-stream grain size fines from upstream (D_{50} of ca. 78 mm and D_{84} of ca. 92 mm, sample size 345) to downstream (D_{50} of ca. 37 mm and D_{84} of ca. 48 mm, sample size 348). The grain size in zones non-inundated at low flow also decreases from a D_{50} of ca. 100 mm close to the glacier terminus to ca. 30 mm in the most braided sector downstream.
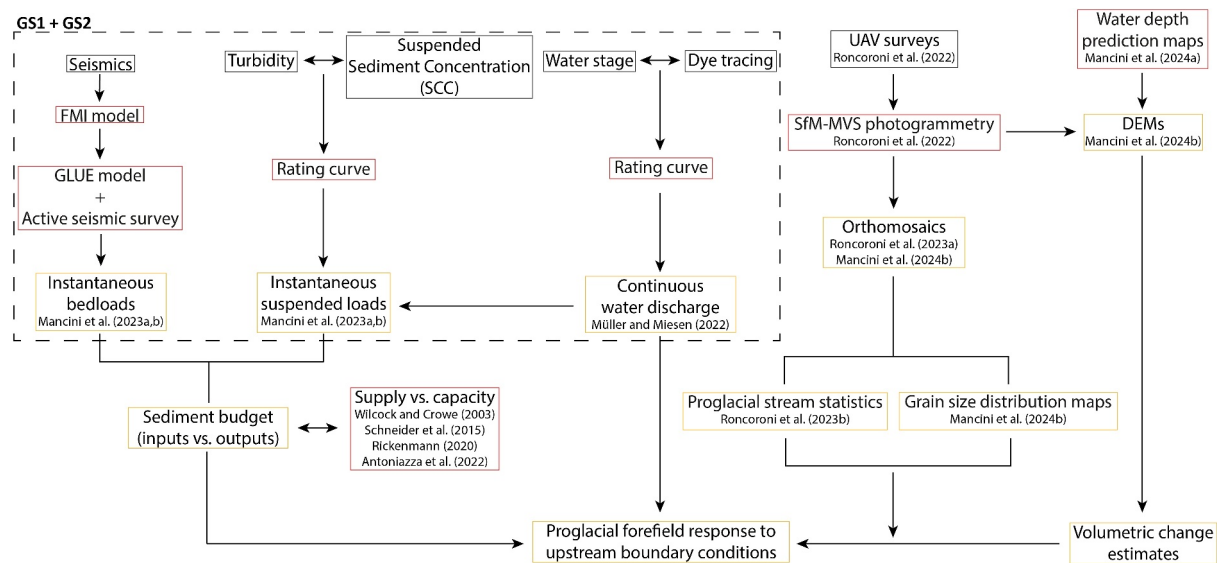
Figure 2. Overview of the methodological approach used in this study. Black boxes are the techniques used in the field, the red ones are those used for the post-processing of the collected data, and the orange ones are the final outputs. The dashed box represents the data measured directly in the field at GS1 and GS2 (Figure 1).

Data were collected for two melt seasons with different climatic conditions: summer 2020 from 8 July [Day of the Year (DOY) 190] to 27 August [DOY 240] which was warmer and drier; and summer 2021 from 12 July [DOY 193] to 21 August [DOY 233] which was wetter especially in the first part of the melt season (Figure S1 Supplementary Information S1).

2.2. Methods

The relationship between upstream boundary conditions and proglacial forefield response was investigated by combining continuous sediment flux quantification, water discharge measurements and repeated daily UAV surveys (Figure 2). Turbidity sensors, geophones and water pressure sensors were deployed at the glacier terminus (Gauging Station [GS] 1) and at the forefield outlet (GS2) for the continuous monitoring of the water stage and both suspended sediment and bedload transport (Figure 1) (Section 2.2.1). The measured bedload transport rates (S) at GS1 were compared to the potential bedload transport capacity (C) estimated using a hydraulic transport model based on the instantaneous discharge to investigate the geomorphic response of the proglacial forefield to under- and over-subglacial sediment supply conditions (Section 2.2.2). If S is higher than C, deposition in the forefield is expected, while in the opposite case erosion is expected. Aerial images of the floodplain, covering the spatial extent shown in Figure 1, were collected daily during low flow conditions using an UAV. Photogrammetric post-processing was used to generate DEMs and orthomosaics of the floodplain for the two melt seasons (Section 2.2.3). The DEMs allowed the determination of volumetric change estimates over time for the entire proglacial forefield (Section 2.2.4). Orthomosaics were used to manually classify the floodplain into inundated and dry regions, a condition needed (a) to extract basic planimetric information on the proglacial stream over time, such as daily braiding indices, total number of bars, and bars total area and perimeter length and (b) to determine the spatial distribution of water depths through the application of a statistical model (Sections 2.2.4 and 2.2.5). Orthomosaics were also calibrated to produce grain-size maps of dry regions at the floodplain scale to investigate surficial texture changes over time (Section 2.2.6). All data sets used in this study have been published and we explain where they can be obtained below.

2.2.1. Sediment Supply to and Export From the Proglacial Forefield

The methods and data sets acquired at GS1 and GS2 have been published in open access format for discharge in Müller and Miesen (2022) and for continuous suspended sediment and bedload fluxes in Mancini et al. (2023a, 2023b).

Daily total suspended sediment load and bedload at the upstream and downstream stations were calculated by cumulating instantaneous loads (unit kg/s) and multiplying these by a measurement resolution of 120 s. The loading was converted into daily volumes and corrected for porosity for comparison with volume of change estimates using:

$$V = \frac{M}{\rho_s \, x \, E} \tag{1}$$

where:

V = daily transported volume [m^3];

M = daily mass of transported sediment [kg];

ρ_s = density of sediment [kg/m^3] = 2650 kg/m^3 (Bezinge et al., 1989); and

E = porosity = (1–0.85) = 0.15 (Carling & Reader, 1982)

2.2.2. Sediment Supply and Potential Transport Capacity

The geomorphic response of the proglacial forefield was investigated for under- and over-subglacial sediment supply (S) conditions compared to the actual theoretic potential capacity (C) of the proglacial stream.

We estimated C for the relatively straight stream pattern just upstream from the start of the braided sector (GS1) using shear-stress based sediment transport equations developed for Alpine streams (Antoniazza et al., 2022; Rickenmann, 2020; Schneider et al., 2015) based on the modified Wilcock and Crowe (2003) approach. The latter allows to compute potential transport rates for particles larger than 0.004 m, which correspond to fine gravel. Consequently, we assume this size is the interface between suspended load and bedload in our study area.

The potential transport rates over the entire channel width were determined from (Antoniazza et al., 2022):

$$Q_b = b * \rho_s * W^* * \frac{(g * r_h * S)^{1.5}}{R * g} \tag{2}$$

where: Q_b = potential bedload transport rate [kg/s]; b = average channel width [m] (i.e. 10 m); W^* = dimensionless transport rate over the entire channel width defined as

$$W^* = 0.002 \left(\frac{\tau^*_{D50}}{\tau^*_{rD50}} \right)^{16.1} \text{ for } \left(\frac{\tau^*_{D50}}{\tau^*_{rD50}} \right) < 1.143 \text{ and } D > 4 \, mm \tag{3}$$

$$W^* = 14 \left(1 - \frac{0.85}{\left(\frac{\tau^*_{D50}}{\tau^*_{rD50}} \right)^{0.7}} \right)^{4.5} \text{ for } \left(\frac{\tau^*_{D50}}{\tau^*_{rD50}} \right) \geq 1.143 \text{ and } D > 4 \, mm \tag{4}$$

τ^*_{D50} = dimensionless bed shear stress defined as

$$\tau^*_{D50} = \frac{r_h S}{R D_{50}} \tag{5}$$

τ^*_{rD50} = dimensionless reference bed shear stress defined as

$$\tau^*_{rD50} = 0.56 S^{0.5} \tag{6}$$

D_{50} = median of the surface grain-size distribution (i.e. 0.078 m); r_h = hydraulic radius [m] defined as

$$r_h = \frac{(b + mh) \, h}{\left(b + 2h * \sqrt{1 + m^2} \right)} \tag{7}$$

h = measured water depth [m]; m = increase in channel width with depth defined as

$$m = \frac{h}{\tan(45)} = 1 \qquad (8)$$

S = channel gradient [-]; R = relative sediment density [-] using sediment (ρ_s) and water (ρ_w) densities set at 2,650 and 1,000 kg/m^3, respectively; and g = gravitational acceleration 9.81 (m/s^2).

Topographical and sedimentological parameter values are available in Mancini et al. (2023b). Forefield evolution was investigated by looking at the relationship between theoretic bedload transport capacity (C) estimates and field-collected bedload sediment supply (S) issued from geophone measurements.

2.2.3. Repeat Digital Elevation Models (DEMs) and Orthomosaics of the Proglacial Forefield

Aerial images of the braidplain were collected once a day during low flow conditions using a DJI Phantom 4 Pro. The survey time in 2020 to do this was long (ca. 3.5 hr) with the potential for changing conditions (light, water discharge, etc.) during data collection. Hence, in 2021, we deployed two UAVs (DJI Phantom 4 Pro) simultaneously. Data collection involved a systematic approach consisting of subdividing the forefield into four sectors, each of that was surveyed using two orthogonal rectangular grids (camera at nadir and flight height of 80 m) and two circular flights (camera pointing in direction of the center and flight height of 60 m) according to best practices given in James et al. (2020) to minimize propagation of systematic errors. Post-processing of collected data sets was performed photogrammetrically in Agisoft Metashape (version 1.5.5) with the aid of field-collected ground control points (GCPs) to generate a time-series of georeferenced orthomosaics and DEMs of the flood-plain for the two melt seasons. The orthomosaics had a resolution of 0.05 m and the DEMs of 0.2 m. Details of data collection and post-processing are available in Roncoroni et al. (2022). Orthomosaics were used to manually classify the floodplain into inundated and dry regions, a condition needed to (a) extract basic planimetric information on the stream (Section 2.2.5), (b) define the surficial grain size distribution (Section 2.2.6), and (c) estimate the spatial distribution of water depths through the application of a statistical model developed in Mancini et al. (2024a). Validation tests for a subset of available data demonstrated that the model was able to reproduce the water depth distribution for braided mountain streams (Mancini et al., 2024a). Elevation uncertainties for permanently inundated and transient regions range from ±0.035 to ±0.060 m, with associated limits of detection (LoD) between ±0.045 and ±0.090 m. These limits are slightly higher than those for permanently dry regions (i.e. ±0.042 and ±0.043 m). Thus, reworking and deposition patterns could be detected for changes smaller than the mean D_{50} (0.06 m) in dry zones; but 1.5 D_{50} in permanently inundated zones. Geomorphic changes in transient regions lie between these two cases. Water depth maps were integrated into DEMs of dry regions to obtain DEMs of the entire proglacial forefield (Westaway et al., 2003). These data sets are available in Roncoroni et al. (2023a) and Mancini et al. (2024b).

2.2.4. DEMs of Difference and Volume of Change Estimates

DEMs were classified according to a contingency table of pixel evolution between surveys (i.e., permanently dry, permanently inundated or transient wet to dry or dry to wet) using the inundation maps described above (see Mancini et al., 2024a). The heuristic model of water depth resulted in spatial variation in the uncertainty of individual water depths; thus, in inundated regions, DEM elevation uncertainty was computed spatially as the sum in quadrature of both water depth prediction and water surface as (Lane et al., 2003):

$$EU_{ij} = \pm\sqrt{\sigma d_{ij}^2 + \sigma e_{ij}^2} \qquad (9)$$

where:

EU_{ij} = elevation uncertainty in cell (i, j);
σd_{ij} = standard deviation of water prediction error in cell (i, j) derived from prediction uncertainty bounds;
σe_{ij} = standard deviation of water surface error in cell (i, j), taken as the dry DEM uncertainty

For dry regions, we used a spatial homogeneous uncertainty value defined as the standard deviation of error computed by comparing 170 field-measured and photogrammetrically reconstructed elevations of stable areas. Thus, Equation 9 is simplified as $EU_{ij} = \sigma e_{ij}$.

DEMs of difference (DoDs) were determined for the active floodplain, the latter defined as the alpha shape of the area experiencing at least one day of morphodynamic change across the two melt-seasons (Roncoroni et al., 2023b). Differences were filtered according by the LoDs set at 95% confidence to highlight only statistically significant geomorphic changes. These were computed as follows (Brasington et al., 2003; Lane et al., 2003):

$$LoD_{ij} = \pm t \sqrt{\left(EU_{ij}^1\right)^2 + \left(EU_{ij}^2\right)^2} \tag{10}$$

where:

LoD_{ij} = limit of detection in cell (i,j) (m);

t = Student's confidence interval threshold (1.96 at 95%), superscripts represent times 1 and 2, respectively

Water depth uncertainties and LoDs for both inundated and dry regions in 2020 and 2021 are available in Figures S2 and S3 of Supplementary Information S1.

Sectoral volumetric change maps were produced from spatially filtered DoD maps and total volumetric change estimates computed following Lane et al. (2003) as

$$V = d^2 n \sum DoD \tag{11}$$

where:

V = Volume (m^3);

d = cell size (i.e., 0.20) (m);

n = number of raster cells in DoD; and

DoD = DEM_{t2}-DEM_{t1} spatially filtered by LoDs (Equation 10).

The associated uncertainties in volume estimates (σv_{ij}) were derived as (Lane et al., 2003):

$$\sigma v_{ij} = \left(\sum_{i=1}^{I} \sum_{j=1}^{J} \left[d_{ij}^2 \left(EU_{1ij}^2 + EU_{2ij}^2\right)^{0.5} \right]^2 \right)^{0.5} \tag{12}$$

To conserve mass, the total daily volumetric difference from the monitoring stations (GS1–GS2) should match the volumetric change derived from the DEMs of difference. However, given the simplicity and the assumptions on which the bathymetric model relies, there is likely to be error and some divergence between the two approaches. We consider this below.

2.2.5. Metrics Describing Forefield Morphodynamics

Daily inundation maps comprised binary matrices (1 for dry and 0 for flooded regions) that allowed extraction of temporal statistics on forefield morphodynamics. The total inundated area was calculated by multiplying the sum of cells having a value of 0 by the pixel area (i.e., 0.0025 m^2). Braiding indices were calculated using a channel count index by determining the number of channels in cross-sections perpendicular to the main valley direction (Ashmore, 1988; Chew & Ashmore, 2001; Egozi & Ashmore, 2008; Hong & Davies, 1979; Howard et al., 1970; Mosley, 1982; Roncoroni et al., 2023b):

$$Bc = \frac{\sum_i^{n_s} n_c^i}{n_s} \tag{13}$$

where:

Bc = braiding index;

Table 1
Calibration Equations of Field-Collected Grain Sizes and Image Standard Deviation to Produce Grain Size Distribution Maps

| | | | Validation | |
| | | | Error [m] | |
Date	Calibration equation	R^2	Mean	STDV
8 July 2020 $n = 30$	$y = 1.653D_{50} - 1.618$ $(R^2 = 0.796)$	0.601	0.003	0.004
11 August 2020 $n = 30$	$y = 1.459D_{50} - 4.875$ $(R^2 = 0.626)$	0.761	−0.001	0.004
17 July 2021 $n = 20$	$y = 0.709D_{50} + 3.137$ $(R^2 = 0.826)$	0.643	−0.001	0.002
8 August 2021 $n = 20$	$y = 2.971D_{50} - 4.569$ $(R^2 = 0.909)$	0.743	0.002	0.008

Note. Validation was performed using independent data. The error column refers to the mean and standard deviation of the error between the measured and the predicted grain-size values.

i = cross-section;
n_c = total number of channels; and
n_s = total number of cross-sections

Inundation maps were used to determine bar characteristics (e.g., bar area) for bars greater in area than 10 pixels (0.025 m^2). The obtained temporal braiding index and mean bar area values were normalized to better highlight the temporal occurrence of high and low peaks when compared to subglacial sediment export magnitudes, and to ease the comparison between fluvial variables. We also generated a summary inundation map following Roncoroni et al. (2023b) to give the number of days that each pixel in the forefield was permanently inundated.

### 2.2.6. Surface Grain-Size Data

Grain-size maps of dry regions at the forefield scale were generated using a texture-based approach calibrated against field collected grain-size samples (Lane et al., 2020). Such an approach assumes that there is a relationship between image properties (e.g., zonal standard deviation of a gray-scale image) and parameters describing the particle sizes present (e.g., D_{50}) (Carbonneau et al., 2004, 2005). Delimitation of individual grains and extraction of grain-size properties (e.g., Butler et al., 2001) is not possible with the available resolution of the orthomosaics. The detailed methodology used to produce grain size maps is available in Figure S4 of Supplementary Information S1.

Calibration data were collected twice for both melt seasons (8 July and 11 August in 2020; 17 July and 8 August in 2021) in 30 randomly selected stable sites of the floodplain using grid-by-number sampling (Wolman, 1954). The four corners of a 1 × 1 m square were measured with a differential GPS (dGPS) and grains were manually sampled at 0.10 m grid intersections within each square. The b-axis of each sampled grain was measured. Those smaller than 0.002 m were recorded as 0.002 m. Squares were split equally between calibration and validation data sets.

The dGPS coordinates were used to identify the corresponding image segment for each grid for which the standard deviation of its greyscale pixel was determined to represent the image texture. This was related to D_{50} in the form $y = aD_{50}$ CE $+$ b. The calibration results are shown in Table 1. The estimates of D_{50} were then assessed for the validation data sets. Table 1 suggests a good agreement between measured and predicted grain-sizes with R^2 values equal or higher than 0.6, negligible mean errors (i.e., bias) and standard deviations of error of between ±2 and ±8 mm. As the calibration used sampled grains (b axes), there is no need to correct for the fact that the surface expression of grains is not necessarily the b-axis as is the case when grain boundaries are mapped directly from imagery (Adams, 1979). These relations were then used to transform entire orthoimages into grain-size maps.

The UAV data collection strategy was designed to minimize the effects of changing light conditions between data sets, but such effects could not be completely avoided. To correct these artifacts, we re-calibrated the grain-size maps using 15,000 image-estimated D_{50} values sampled in stable zones characterized by different grain sizes where the surficial granulometry should not have changed between surveys (Figure S4 in Supplementary Information S1). The corrected grain-size maps were visually checked leading to some data sets being excluded due to residual texture-related errors (most commonly when lighting conditions had evolved within a survey, such as
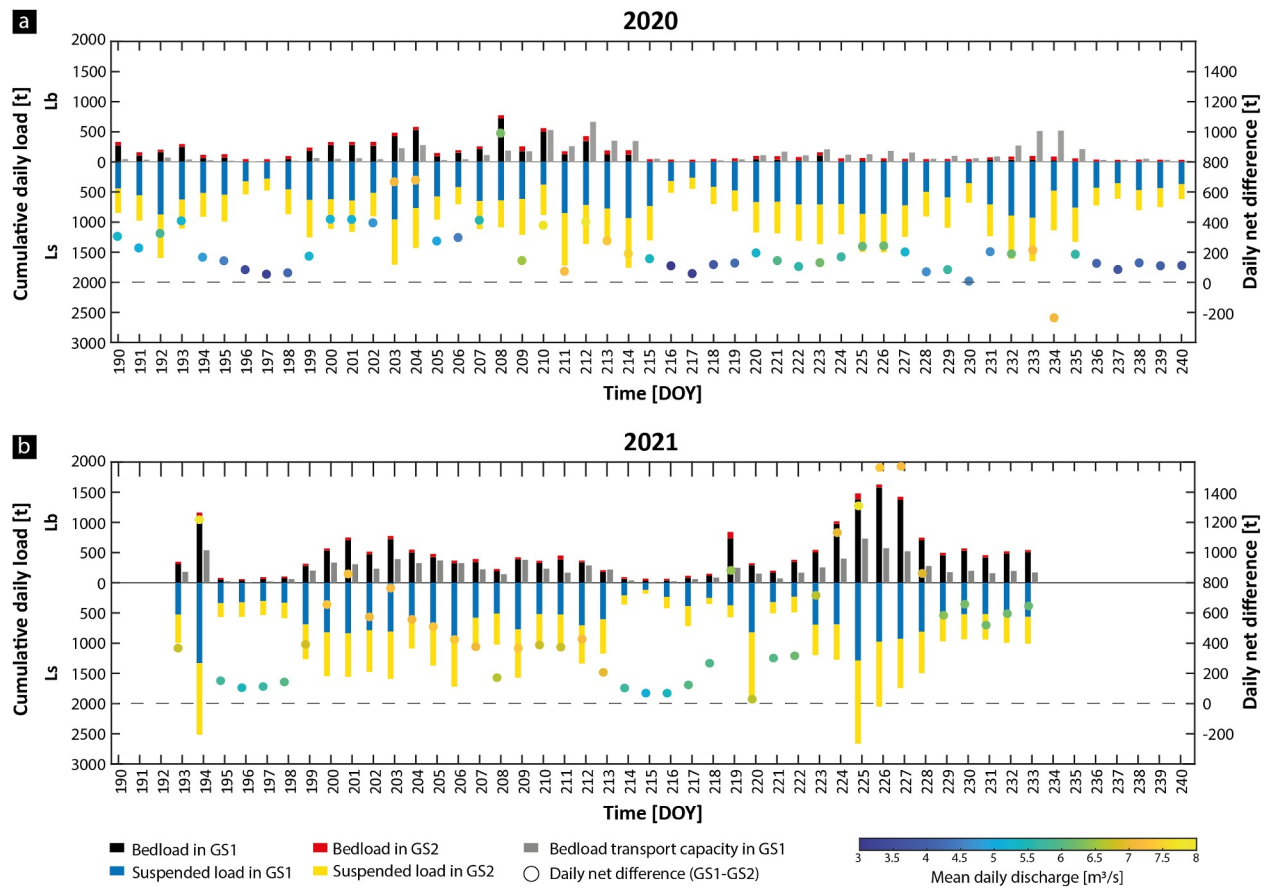
Figure 3. Daily cumulative sediment loads (suspended sediment [Ls] and bedload [Lb]) at GS1 and GS2, net load difference in relation to daily mean discharge rate, and bedload transport capacity measured in GS1 (Equation 2) for melt seasons 2020 (a) and 2021 (b). Day of the year [DOY] refers to the number of days since 1 January. Instantaneous and cumulative sediment quantifications and relative uncertainties are available in Figure S5 of Supplementary Information S1, while discharge records in Müller and Miesen (2022).

due to changing cloud cover). At the end of this filtering, a total of 6 (26 July [DOY 208] to 27 August [DOY 240]) and 4 (22 July [DOY 203] to 12 August [DOY 225]) data sets for, respectively, 2020 and 2021 were retained and used to investigate the spatial patterns of grain-size changes. As with the DoDs, we limited the grain-size difference maps to the extent of the active floodplain. Following Lane et al. (2020), we identified a limit of detection for grain-size changes, computed from 350 points randomly sampled in stable zones (Figure S4 in Supplementary Information S1). These data sets are published in Mancini et al. (2024b).

Grain-size difference maps were compared to elevation difference maps, both spatially and by converting them into bi-dimensional frequency plots. The sub-daily and weekly grain-size and elevation of difference maps were masked by inundation maps (see Section 2.2.5) to exclude the wetter surface from the analysis. To produce bi-dimensional frequency plots, elevation changes were classed at cm resolution between −0.55 and +0.55 m; and grain-size changes at a cm resolution between −0.065 and +0.065 m. This analysis allowed the determination of the relationship between erosion/deposition and fining/coarsening and its visualization.

3. Results

3.1. Total Sediment Loads at GS1 and GS2 and Their Relationship With Transport Capacity

The proglacial margin experienced different total sediment transport loads in the two melt seasons under investigation (Figure 3). The daily mean amounts of glacier subglacial sediment load (GS1 in Figure 1) were 719.4 ± 120 t (2020) and 1,052.2 ± 462 t (2021), while the downstream export at the forefield outlet (GS2 in Figure 1) was much lower, with daily means of 533.7 ± 21 t (2020) and 571.7 ± 68 t (2021). These data imply net

aggradation greater in 2021 than 2020 (Figure 3). Only one day, DOY 234 in 2020 recorded the proglacial margin as a sediment source.

Daily suspended sediment loads (Ls) had a strong Pearson correlation with discharge at both GS1 ($r = 0.695$, $p < 0.05$, in 2020 and $r = 0.786$ $p < 0.05$, in 2021) and GS2 ($r = 0.651$, $p < 0.05$, in 2020; $r = 0.768$, $p < 0.05$ in 2021), suggesting that these are hydrologically driven in both locations. Daily bedload transport rate (Lb) correlations with discharge were only significant at GS1 in 2021 ($r = 0.466$, $p > 0.05$, in 2020; $r = 0.681$, $p < 0.05$, in 2021), while at GS2 they are lower in both melt seasons ($r = 0.425$ in 2020, $p > 0.05$; $r = 0.286$ in 2021, $p > 0.05$). Weaker correlations between discharge and daily bedload rates within the proglacial forefield imply a greater probability that on a daily basis there is an imbalance between S and C. Cumulative load uncertainties for both Ls and Lb are provided in Figure S5 of Supplementary Information S1.

In 2020, there were two different periods in terms of bedload transport balance (Figure 3a). Between DOY 190 and ca. DOY 210 to 215, *S* exceeded *C* with the subglacial channels delivering coarser material than the proglacial stream could transport. This is reflected in the measured bedload balance with a total of 5,551 (3,813 to 8,357) t of bedload entering the forefield until DOY 215 at GS1, whilst 1,384 (1,344 to 1,921) t (24.9%) left the forefield at GS2. A total of ca. 4,168 (2,469 to 6,536) t of bedload accumulated in the proglacial margin. For the same period, 2,560 (2,410 to 2,829) t of suspended sediment was stored in the forefield. After DOY 215, S became lower than C, ca. 452 (192 to 1,813) t (−91.8%) of bedload supplied at GS1 but ca. 1,157 (1,114 to 1,584) t leaving at GS2 and ca. 663)240 to 965) t leaving the reach. However, the suspended load continued to accumulate, with a net 3,470 (3,160 to 3,570) t of suspended sediment deposited. Thus, there was overall net deposition throughout 2020, both bedload and suspended load until DOY 215 and then through suspended load deposition exceeding bedload loss after DOY 215.

In 2021, S generally remained higher than *C*, which should result in a continuous phase of aggradation throughout the melt season (Figure 3b). Until ca. DOY 220, S was only slightly higher than C. Bedload inputs to GS1 were ca. 9,136 (3,274 to 13,600) t and loss through GS2 was ca. 1,116 (249 to 1,917) t (12.2%), implying that ca. 8,020 (3,025 to 11,653) t of bedload were stored in the proglacial margin. This compares with 2,100 (1,820 to 2,230) t of suspended load. From DOY 220, the difference between *S* and *C* increased; the total bedload supply to GS1 increased to ca. 9,743 (4,542 to 13,180) t, but the downstream export through GS2 reduced to 593 (163 to 1,203) t. Consequently, ca. 9,150 (4,379 to 11,986) t of bedload were stored. This compares with 5,488 (4,628 to 6,178) t of suspended load.

3.2. Forefield Geomorphic and Morphodynamic Response

To understand how the forefield is related to these changing sediment supply and export conditions, we considered the spatial (laterally integrated) and temporal patterns of channel change together with the number of days the reach was inundated (Figures 4a and 4b), the temporal evolution of volume change (Figures 4c and 4d) and the cumulative volumes of sediment stored in the reach according to the DEMs and the load data (Figures 4e and 4f).

Rates of riverbed reworking were greater during summer 2021 as compared to 2020 (Figures 3, 4a, and 4b and Figure S6 in Supplementary Information S1). Geomorphic changes were most notable in the most braided sector. The upstream end of this braided sector was ca. 300 m downstream of GS1 in 2020 (Figures 4a and 4b), with a major flow divergence region and where there is a decrease in valley bottom slope (Figure 1). The braided zone is at its maximum width 550 m downstream (Figures 4a and 4b) and then converges to be a single thread 800 m downstream.

Figure 5 shows the geomorphic responses to the balance of *S* and *C* for these two regions. For the two periods with $S > C$, there were higher deposition rates most notably between 500 and 700 m downstream in the braided sector. During 2020, there was an avulsion to the true right between 300 and 500 m downstream and the most intense deposition between 500 and 700 m was downstream of the post-avulsion channel (Figure 5a). For the period in 2020 where $C > S$ there is clear evidence of incision in the main channel from GS1 through to 500 m downstream (Figure 5b). Qualitatively, deposition patterns appear to coincide with flow divergence regions and erosion patterns with regions of maximum channel curvature and flow convergence areas (Figure 5 and Figure S6 in Supplementary Information S1). One large bar 550–650 m downstream remained present throughout the study, with reworking happening around it (Figure 5).
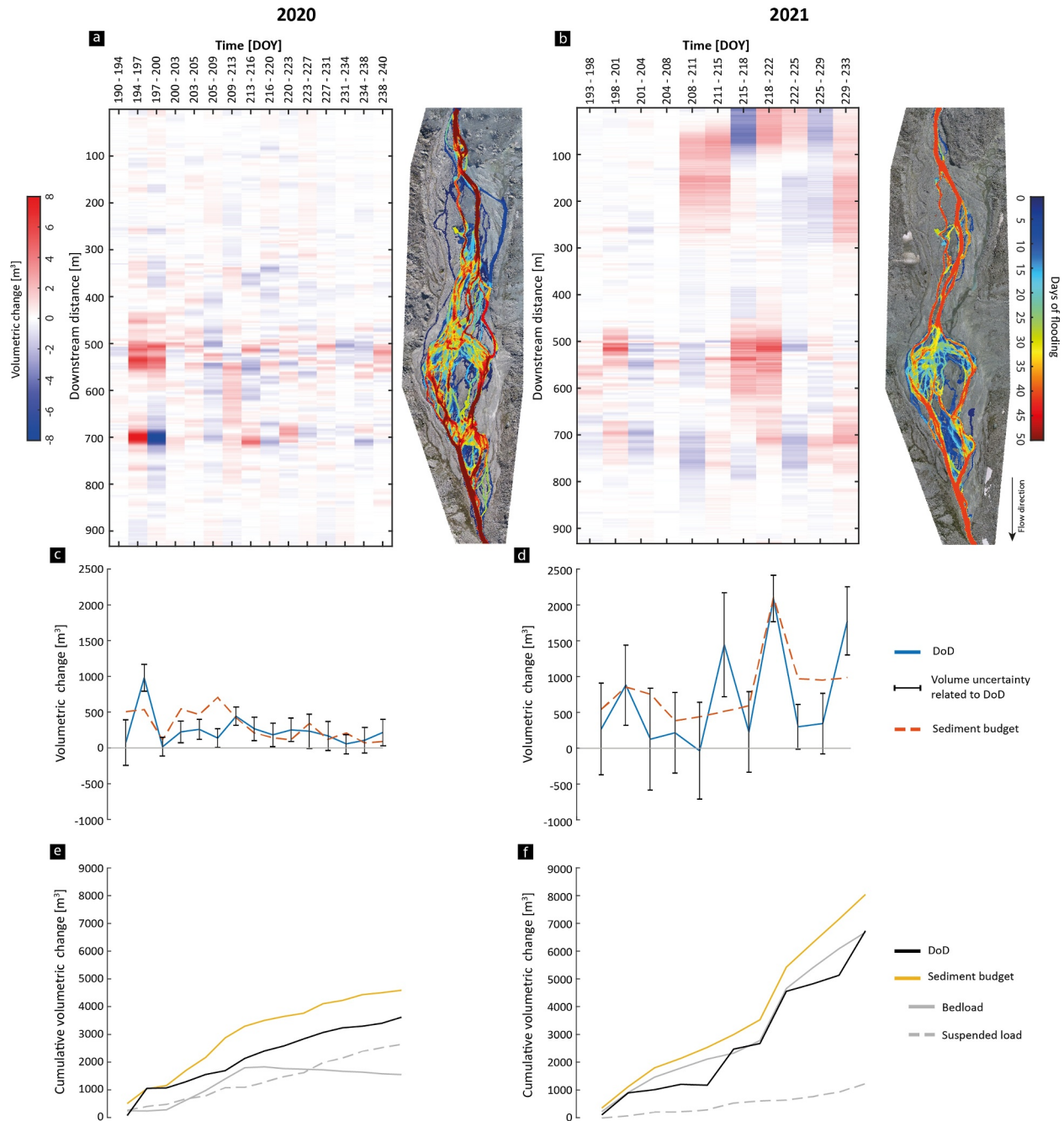
Figure 4. (a and b) 2D volumetric change maps in relationship with the spatial distribution of flooding frequencies in the two melt seasons; (c and d) volumetric changes issued from temporal DEMs of difference (DoD) (blue line) and total volumetric sediment budget (GS1–GS2, orange dashed line); (e and f) cumulative sediment budget (GS1–GS2) according to DoD calculations and sediment load records (total sediment, suspended sediment and bedload). Limits of detection values used in DoDs are available in Figure S2 of Supplementary Information S1 (wet regions) and Figure S3 in Supplementary Information S1 (dry regions), field-collected instantaneous and cumulative transport rates for both suspended sediment and bedload (with uncertainties) in Figure S5 of Supplementary Information S1, while elevation of change maps in Figure S6 of Supplementary Information S1.

Both volumetric and the load-based methods suggest that the forefield is storing subglacially exported sediment (Figures 4e and 4f). The temporal evolution of volumetric changes follows the same trend as the sediment budget (Figures 4c and 4d), but with a relative tendency for the DEM method to underestimate the volume of sediment being stored in the reach.
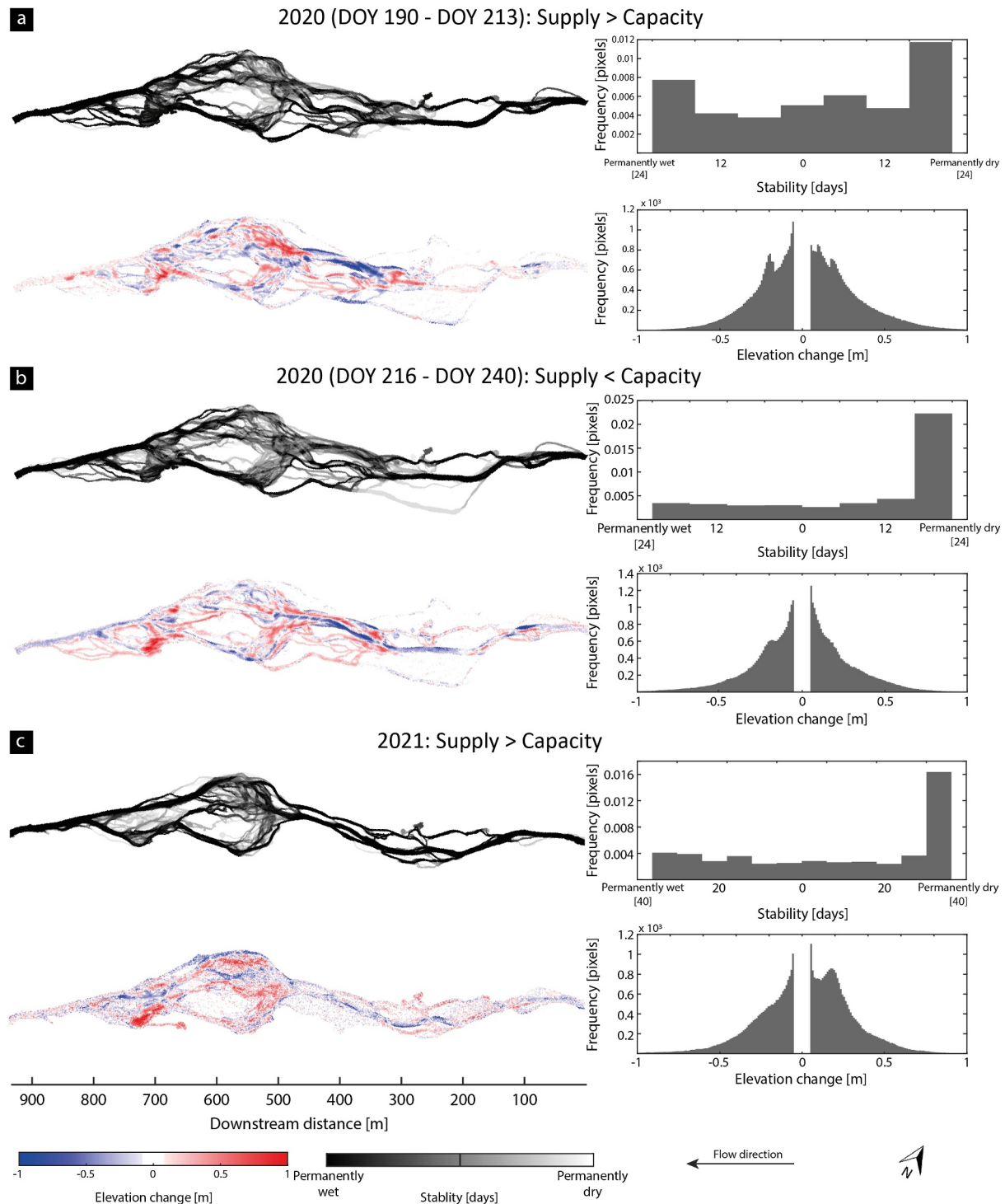
Figure 5. Seasonal frequency of inundation (upper), elevation of change (lower) maps and associated frequency histograms for different supply transport conditions in melt seasons 2020 (a and b) and 2021 (c). Inundation maps are issued from flooding frequency maps (Figures 4a and 4b and Figure S7 in Supplementary Information S1), while elevation of change maps for smaller temporal intervals are available in Figure S6 of Supplementary Information S1. Limits of detection values are available in Figure S3 in Supplementary Information S1.
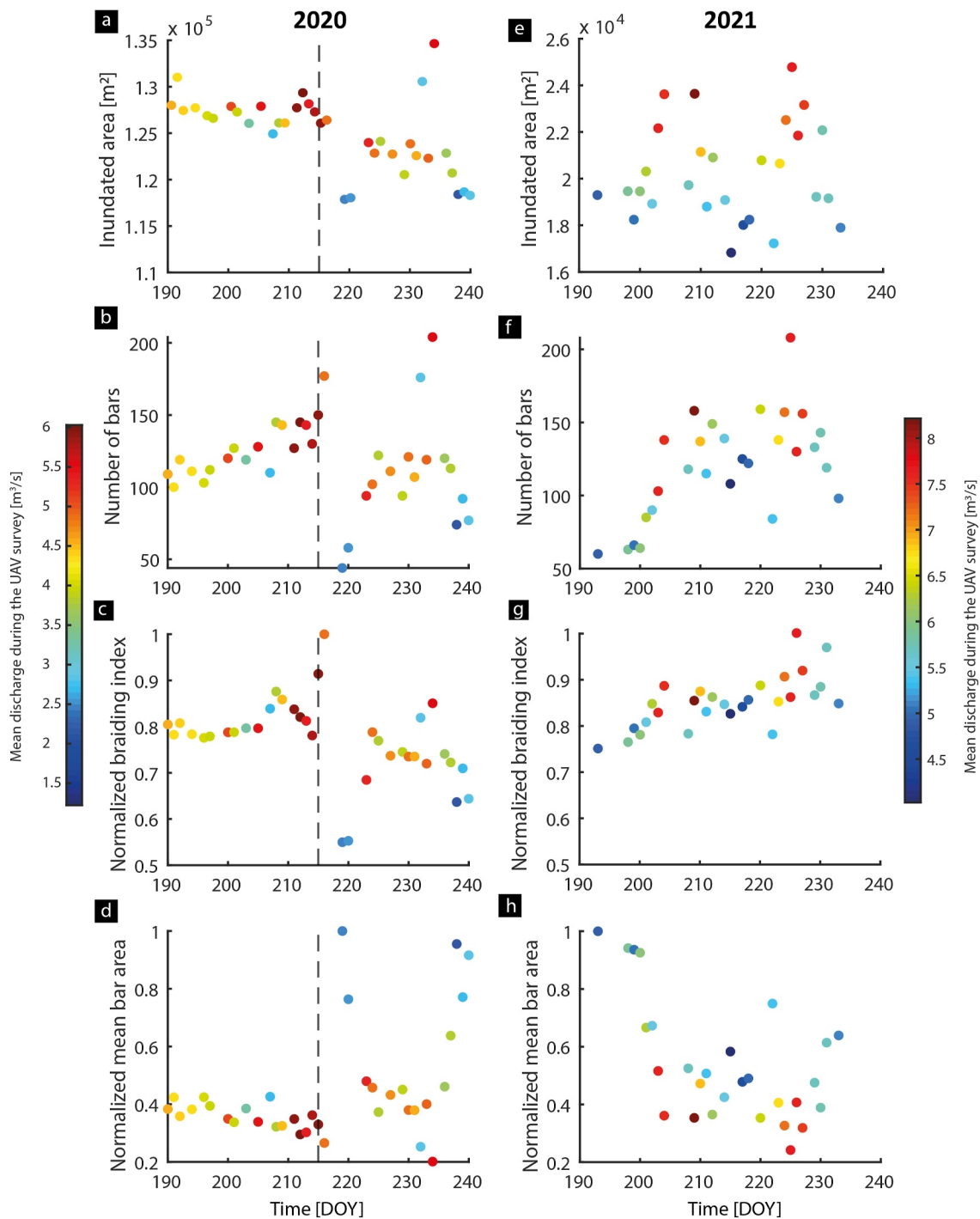
Figure 6. Proglacial stream statistics for melt seasons 2020 and 2021. Total inundated area (a–e), number of bars (b–f), normalized braiding index (c–g) and normalized mean bar area (d–h). Absolute braiding index values are comprised between 2 and 4.5 (2020) and 3 to 4.5 (2021), while absolute bar area is between 100 and 600 (2020) and 80–350 m^2 (2021).

Channel patterns respond to these volumetric changes. From 2020 until DOY 215, when $S > C$, the total number of channels, the normalized braiding index and the number of bars increased (Figures 3a and 6). Bars became smaller with a concomitant increase in the number of flow convergence and divergence regions (Figure 6c, Figure S7 in Supplementary Information S1).
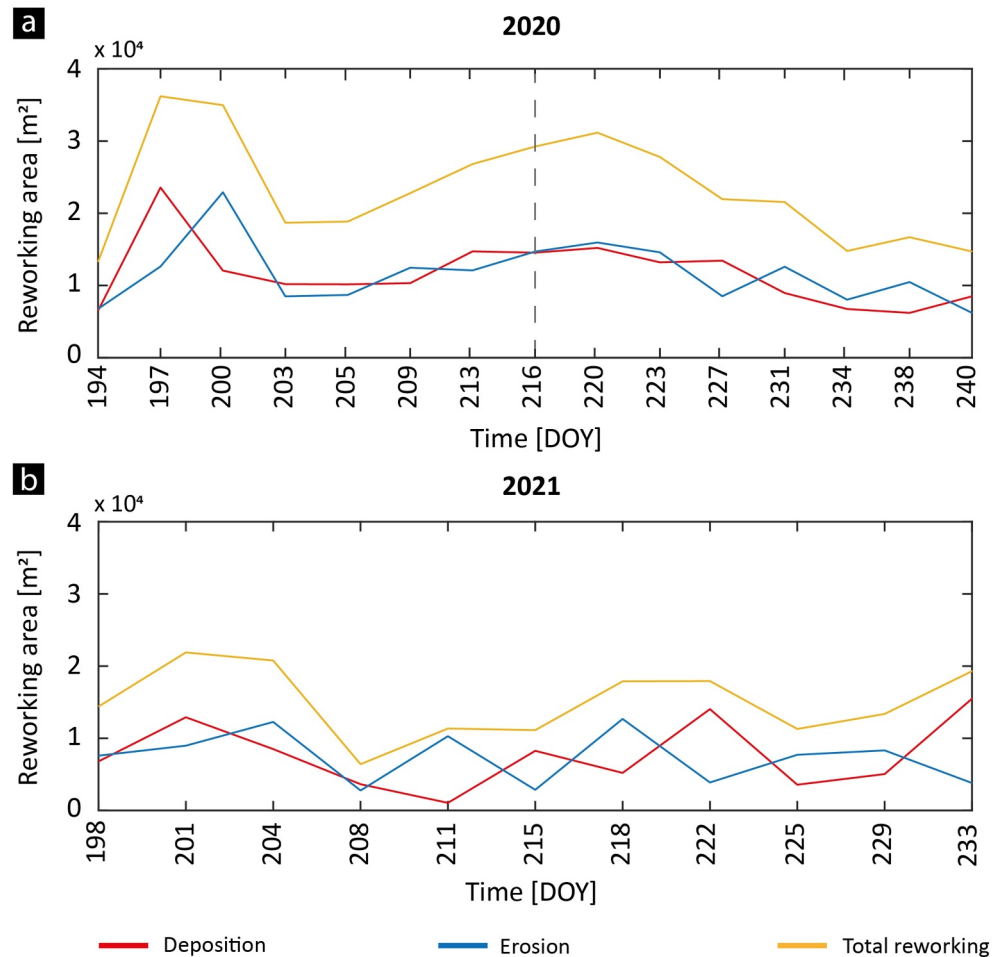
**Figure 7.** Reworked area (deposition, erosion and total) associated with volumetric change quantifications (Figures 4 and 5) for melt seasons 2020 (a) and 2021 (b). The dashed gray line in (a) marks the change from $S > C$ to $S > C$ conditions. Elevation surface maps used to retrieve the reworking extent are available in Figure S6 of Supplementary Information S1.

Despite the sensitivity to changes in discharge, the inundated area was high during this period (ca. 1.27×10^5 m^2) and ca. 3.7×10^4 m^2 (ca. 19.2% of the active floodplain) experienced reworking processes (Figures 6a and 7a and Figure S7 in Supplementary Information S1). During this period, the proglacial forefield underwent a total aggradation of ca. 2,300 m^3, most of which was associated with zones passing from wet to dry (ca. 3,320 m^3, Figure 8a). Dry (during measurement) regions had erosion and deposition in balance. The downstream supply to GS2 was sustained by transient regions passing from dry to wet and by permanently inundated areas be reworked, respectively, ca. 350 and ca. 530 m^3 of material (Figure 8a).

When $C > S$ from DOY 215 in 2020 and there was channel incision upstream (Figure 5b); eroded sediment as well as that supplied from the glacier was insufficient to maintain the same braiding intensity in the braid zone; bars increased in size and total number and the braiding index decreased with the flow increasingly confined to fewer channels (Mann-Kendall tests at $p < 0.05$ confirmed monotonic trends; Figures 6a–6d and Figure S7 in Supplementary Information S1). The total area being reworked progressively decreased to ca. 1.4×10^4 m^2, constituting around 7.3% of the total active floodplain (Figure 7a). The sediment budget data suggest that the forefield continued to act as a sink for suspended load (ca. 1,600 m^3) but, at the same time, ca. 250 m^3 of bedload was removed from the proglacial margin system (Figure 4e). The morphological method suggested a total aggradation of ca. 1,350 m^3 (Figure 4c). Erosion occurred in regions passing from dry to inundated (ca. 600 m^3), while the contribution of permanently inundated areas was limited to 200 m^3. Deposition occurred in regions becoming dry to a total of ca. 2,200 m^3 (Figure 8a).
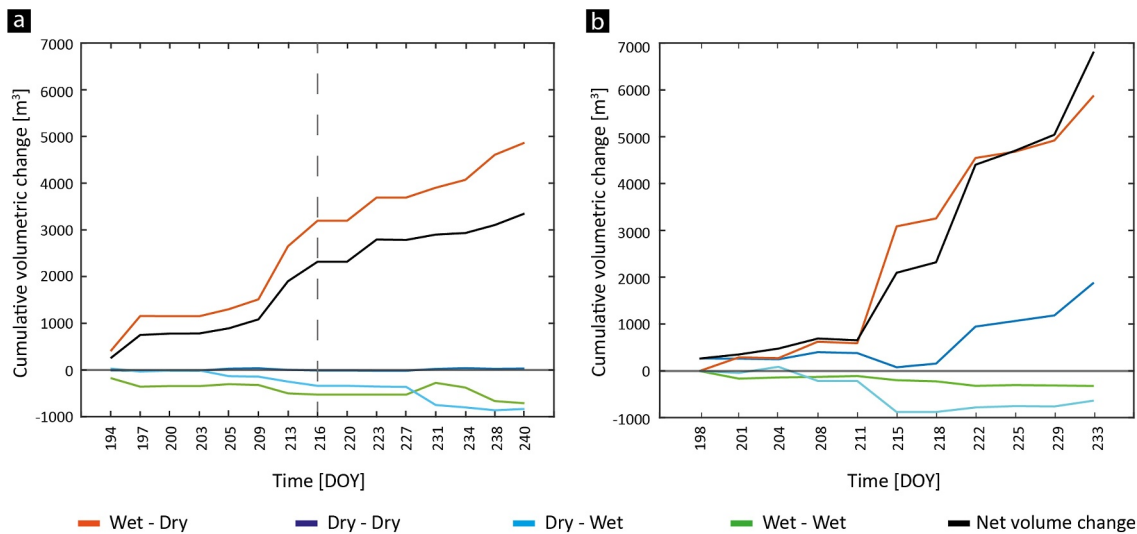
Figure 8. Cumulative volumetric contribution of permanently inundated (green line), permanently dry (blue line) and transient regions passing from inundated to dry (red line) or dry to inundated (light blue line) to the total volumetric change (black line) in 2020 (a) and 2021 (b). The dashed gray line in (a) marks the change from $S > C$ to $S > C$ conditions. DoD maps used to extract the total number of cells associated with these regions are available in Figure S8 of Supplementary Information S1.

In 2021, S was continuously higher or comparable to C. Despite a larger variability due to higher daily discharge amplitudes, the seasonal-scale geomorphic response of the proglacial forefield was similar to the first part of the 2020 melt season with progressively increasing braiding and numbers of bars and falling mean bar area (Mann-Kendall tests at $p < 0.05$ confirmed monotonic trends; Figures 6f–6h). However, the area affected by geomorphic processes was more confined compared to 2020, which, except between DOY 208 and DOY 215, remained constant at around $2.1 \times 10^4 \, \mathrm{m}^2$ (ca. 10.9% of the active floodplain). The proglacial margin stored ca. 6,800 m^3 of sediment according to morphological calculations and 8,100 m^3 according to sediment load data across the entire season (Figure 4f). Of this total ca. 50% occurred in the second part of the melt season (ca. DOY 220 to DOY 234) during high rates of subglacial sediment supply (Figure 4b). Thus, while volumetric changes were more limited in space, their magnitude was higher compared to 2020. Deposition dominated in regions experiencing inundation only during high flow conditions (i.e., permanently dry regions in Figure 8) and in those passing from wet to dry. Erosion was found in the permanently wet zones and those passing from dry to wet, the latter being dominant (Figure 8b). During the second half of the 2021 season, when S increases notably, deposition increased in zones that were previously not inundated upstream of the most braided sector and also through the construction of numerous small bars, accounting for, respectively, 85% and 15% of the total aggradation of ca. 6,100 m^3 in this period (Figure S6 in Supplementary Information S1). The forefield configuration progressively evolved toward a more complex spatial configuration in terms of stream statistics (Figure 6). The periods DOY 194 to 213 and DOY 220 to 228 experienced increasing subglacial bedload evacuation rates, resulting in a downstream increase in the total number of bars, a decrease in their emerged area and, consequently, a higher number of secondary channels (Mann-Kendall tests at $p < 0.05$ confirmed monotonic trends; Figures 3b and 6). The reverse occurred between DOY 214 and 219 and after DOY 229 due to decreasing subglacial supply of coarse particles likely due to colder atmospheric conditions (Mann-Kendall tests at $p < 0.05$ confirmed monotonic trends; Figures 3b and 6 and Figure S1 in Supplementary Information S1).

3.3. Relationship to Changes in Surface Grain-Size Distribution

Figure 9 shows the mean elevation change and surficial grain size change in both melt seasons (Figure S9 in Supplementary Information S1). According to the gauging station data, forefield aggradation persisted throughout both melt seasons, although notable changes, particularly in 2020, were observed in terms of the associated size fractions. The relationship between vertical elevation and surficial grain size dimention (GSD) change (Figures 9a and 9b) shows that summer 2021 experienced more intense grain-size change.

In 2020, up to ca. DOY 219 when $S > C$, the mean elevation change tends to vary between ca. 0.01 and 0.04 m/d and is associated with a general coarsening of surficial sediment deposits of up to ca. 15 mm/d (Figure 9a). This
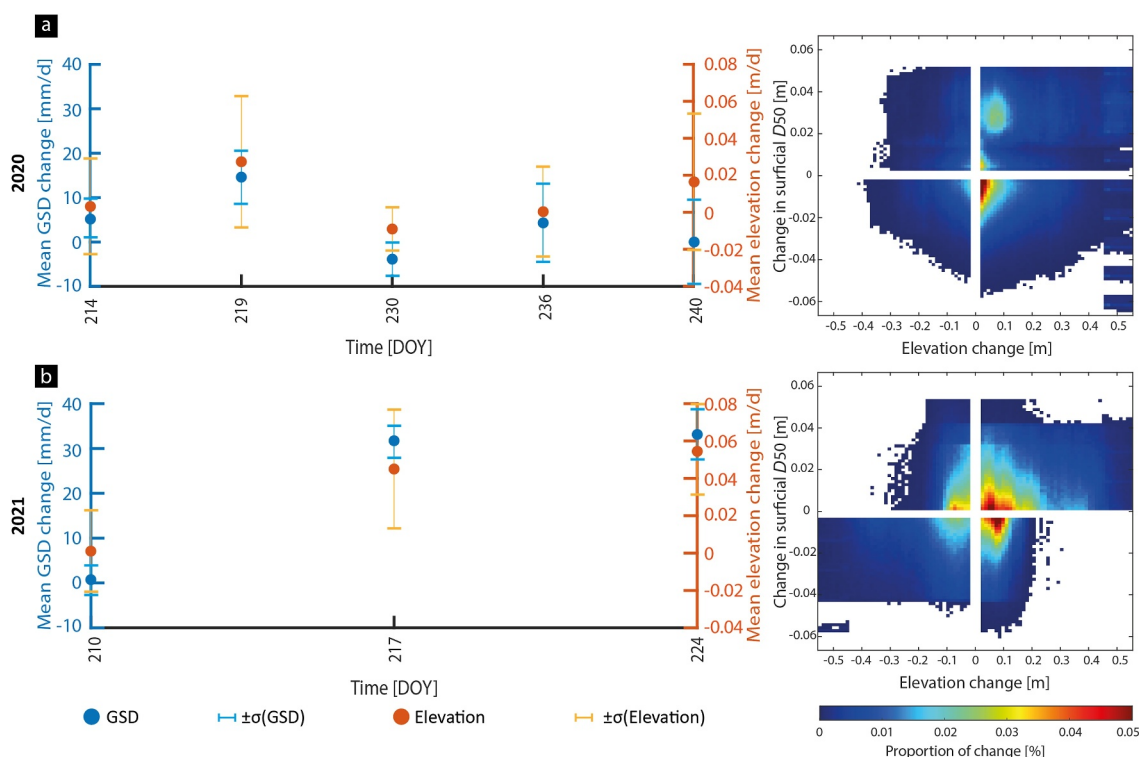
Figure 9. Mean surficial elevation and mean D_{50} rate of change (per day) in 2020 (a) and 2021 (b) melt seasons, with respective proportional change at the seasonal scale.

situation is reflected in the forefield with coarsening on bar heads, especially where the stream initiates braiding, and with a progressive downstream fining toward the forefield outlet (Figure 10a). The situation changed when C became higher than S, with a net decrease of aggradation rates down to ca. −0.02 to 0.02 m/d and with grain size fining between ca. −5 to 1 mm/d (Figure 9a). However, the spatial distribution of change shows two different patterns: aggradation related to coarsening on the right side of the forefield where the stream is more dynamic, with general fining on the most stable left side (Figure 10b). In contrast, in 2021, the evolution related to the mean grain size and elevation change relationship is positive, highlighting the importance of the ratio between coarse and fine sediments exported from subglacial channels in determining the spatial configuration of surficial deposits (Figure 9b).

4. Discussion

4.1. Proglacial Geomorphic Response to Upstream Boundary Conditions

Quantification of sediment flux dynamics from the continuous monitoring of river loads and the repeated elevation difference maps gave comparable results in cumulative terms over long timescales (Figure 4). This coherence not only validates the method presented in Mancini et al. (2024a) for estimating river-bed elevations in the inundated zones of proglacial streams but also gives confidence to seismically inferred bedload flux quantifications (Mancini et al., 2023b; Figure 3). That said, sediment budgets obtained from the two methods differ, which could arise from four possible reasons. First, the bathymetric model used to generate DEMs of both dry and wet regions currently accounts for approximately 50% and 60% of the spatial variability in water depth (Mancini et al., 2024a). Mancini et al. noted that this may be due to an insufficient number of water depth measurements and their correction for changing water stage conditions during the calibration process. Consequently, some prediction errors may propagate into estimates of temporal volume changes derived from DEMs of differencing. Second, the seismic method may have a lower sensitivity to fine sediment fractions (0.002–0.008 m) transported either in suspension or as bedload depending on flow conditions (Wilcock et al., 2009). The net change estimates for suspended and bedload (i.e., the sediment budgets) were lower than those from the DEMs of difference. As there is clear downstream fining in the reach, there may be finer material in transport downstream, such that the seismic method under-estimates how much bedload has left the reach. This would explain why the sediment
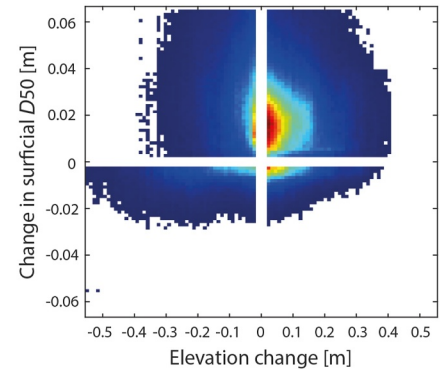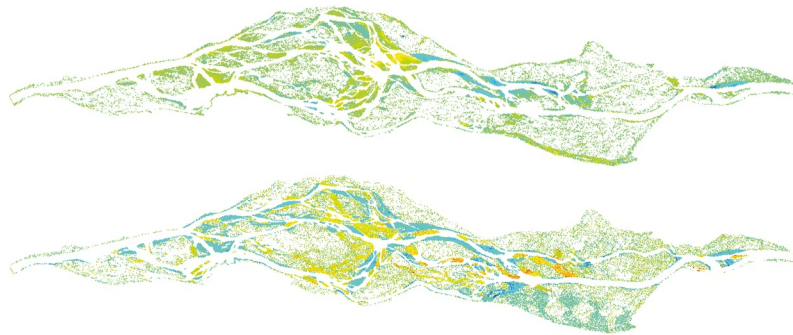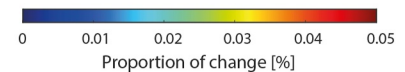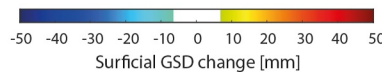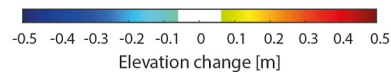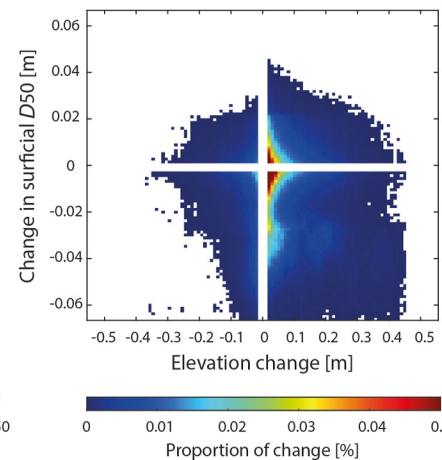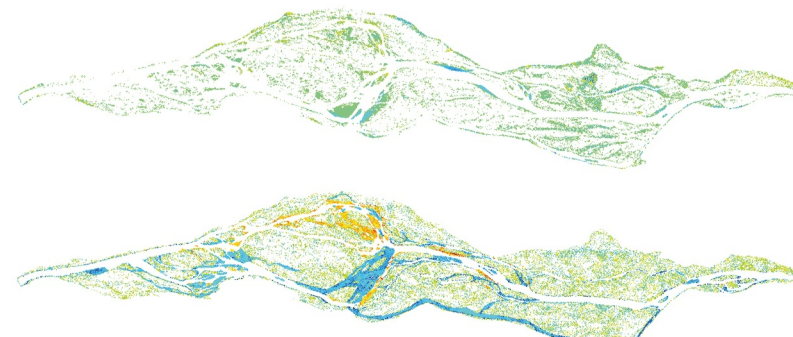
Figure 10. Elevation change (upper maps), surficial grain-size change maps (lower maps) and proportion of change (total number of cells) considering both variables for different sediment supply (*S*) and transport capacity (c) conditions shown in Figure 3. In (a) the example for the 26 July (DOY 208) to the 1 August (DOY 214) 2020 period having S_{ti} exceeding C_{ti}, while in (b) the example for the 23 (DOY 236) to the 27 August (DOY 240) 2020 period characterized by the contrasting condition. Used limits of detection values are given in Figure S4 of Supplementary Information S1, while comparisons over shorter periods are available in Figure S9 of Supplementary Information S1.

budgets have higher estimates of aggradation. Third, the use of LoD thresholds in temporal volumetric changes from DEMs of difference maps to remove non-statistical elevation changes may lead to underestimation (Anderson, 2019). This is because not all elevation changes falling within the LoD range can be attributed to the propagation of random errors due to the photogrammetric process, and some of them may still reflect real geomorphic changes. Finally, fourth, the sediment density and porosity values used to convert sediment transport loads into volumes (Equation 1) are not based on direct field measurements but rather on the literature. The use of a single values retrieved in different geomorphic settings, combined with the spatially in grain size distribution in the study area (Figure 1), may be another source of error for the discrepancy between the two quantifications (Frings et al., 2011; Manger, 1963; Tabesh et al., 2022).

Changes in the upstream supply of sediment, that is, from the glacier, elicit a clear morphodynamic response and the bedload supply matters more than suspended sediment (Figure 6; Ashmore, 1991b; Nicholas et al., 1995). Where supply exceeds capacity at the entrance of the forefield, as for the first part of 2020 and for the entire 2021 melt season, the forefield aggrades where valley slope was lowest (Figure 4). As long as supply exceeded capacity, braiding indices were maintained or increased; the total number of bars tended to decrease; bars became smaller and total inundated area increased (Figure 6; Ashmore, 1991b; Nicholas et al., 1995). In parallel, there was a general coarsening of surface grain size at the forefield scale, but this was limited to bar head regions (Figure 10a). As in this case all supplied sediment was subglacially exported, it appears that bedload supply by the

glacier drives the braiding process. In 2021, the subglacial sediment supply rates were higher than transport capacity for most of the summer season and were associated with substantial deposition in the steeper upstream part of the forefield (Figure 4b). Aggradation is known to lead to increasing braiding intensity, with a reduction in the valley bottom slope upstream and an increase downstream in the region where deposition occurs (Curran et al., 2017; Germanoski & Schumm, 1993; Roussel et al., 2018). In proglacial forefields, our data show that the balance between changes in bedload sediment supply and transport capacity drives the aggradation process and the resulting channel patterns.

When supply is lower than transport capacity, as was the case for the second part of the 2020 melt season, erosion dominated closer to the glacier terminus with stream incision (Figure 5b; Liesle et al., 1993). The proglacial margin continued to act as a sink for suspended sediments, but significant bedload was removed from the forefield (Figures 3a and 4e). Given the extremely low rates of bedload transport supply to the forefield (Figure 3a), the bedload leaving the system is likely to have been released by changes in channel pattern and incision (Germanoski & Schumm, 1993; Marren, 2002; Roussel et al., 2018). The proglacial forefield evolved toward a less complex and a geomorphologically more stable configuration characterized by fewer channels and increasing bar areas, likely to promote the longitudinal connection of sediment flux (Figure 6). Flood inundation maps showed that the forefield was still affected by some large-scale re-organization events, but these were confined to specific sectors (Figure 5b). Changes in surficial grain size distribution maps suggest a general surficial fining due to continued deposition of fines. This is evident as fines constitute a larger proportion of the total volumetric loads, and coarsening patterns occur in the most dynamic sectors (Figure 10b; Asselman & Middelkoop, 1995).

The above observations confirm our initial hypotheses that with ongoing glacier retreat, forefield response is a function of the ratio of sediment supply to sediment transport capacity (Collins, 2008; Guillon et al., 2018; Kaser et al., 2010; Zhang et al., 2022): the dividend of increased runoff during glacier retreat may increase sediment transport capacity drastically, but morphodynamic response depends on whether or not there is concomitant increase in the supply of bedload-sized sediment due to increase in glacial sediment export. Results suggest a strong sensitivity of channel patterns to this balance (Figure 6). The forefield acted as a suspended sediment sink throughout, but bedload responded to the interactions between changing bedload sediment supply and changing sediment transport capacity (Figures 3 and 6). The regions which contributed the most to capturing subglacially exported sediment were those transitioning from wet to dry, while the reworking from areas becoming inundated was less important (Figure 8). This suggests that the reworking of deposited coarse particles was difficult once they were in place. This reworking also strongly affected the bedload evacuation from the reach and explains the strong filtering for this reach reported by Mancini et al. (2023b). There is also a methodological issue to note. Figure 3 shows that the relationship between the transport capacity and discharge is not linear. There are days with higher discharge rates that are not always associated with the largest bedload transport capacities. This discrepancy may be attributed to the constant D_{50} value of 0.078 m used in the capacity model, which does not accurately reflect the entire range of bedload fractions effectively transported in proximity to GS1. Further studies are needed to better address the relationship between subglacial sediment evacuation and proglacial forefield response.

4.2. Implications for Downstream Sediment Transport

The strong relationship between subglacial bedload export, morphodynamic activity and forefield geomorphic evolution contrasts with that of suspended sediment load (Figure 3). When the upstream bedload supply is higher than the transport capacity, lateral erosion appears to predominate over the vertical component as, due to aggradation, higher proportions of dry regions are reworked to maintain the discharge rate (Antoniazza et al., 2019). This phenomenon is particularly evident during the 2021 melt season (Figure 8b). At the same time, the increasing braiding intensity combined with the establishment of flow divergence regions causes the forefield to become more of an obstacle to downstream transported particles (Ashmore, 1988; Ferguson & Ashworth, 1992; Kasprak et al., 2015). An aggrading proglacial margin likely increases its tendency to be a sediment sink (Figures 4e and 4f).

In contrast, when transport capacity becomes greater than upstream supply, as in the second half of 2020, the forefield contracts into fewer channels likely to create hydraulically more efficient channels, which in turn progressively reinforces the erosional tendency, especially for the vertical component increase in bedload export from the proglacial forefield (Ashmore et al., 2011; Bertoldi et al., 2009; Egozi & Ashmore, 2009). Sediment

reworking can only influence bedload export directly if discharge variations are sufficiently high to reach the characteristic critical discharge (Q_c) for a sufficiently long period of time ($t_{Q > Q_c}$) both to entrain and to export previously deposited bedload particles (Ashmore, 1982; Mancini et al., 2023b; Parker, 1979). In our case, this occurred at the beginning of August 2020 (ca. DOY 220) when daily hydrographs were already characterized by high daily maximum discharges, giving both the competence to entrain sediment and the capacity to move it downstream (Figures 3a and 10b; Lane & Nienow, 2019; Mancini et al., 2023b).

4.3. Wider Implications

Our results suggest that proglacial forefields respond to changes in bedload-sized sediment supply, with aggradation and enhanced morphodynamic activity, modifying the surficial grain size distribution, and storing and buffering the downstream flux of upstream delivered sediments. As glaciers retreat, the balances between bedload sediment supply, both its erosion by subglacial processes and its transport under the ice, and transport capacity will both change (Li et al., 2021; Zhang et al., 2022, 2023) and are likely to lead to systematic shifts in river channel pattern. As glacial erosion rates have a dependence on ice thickness through the latter's control on ice velocity (Cook et al., 2020; Herman et al., 2015), there is likely to be a progressive decline in bedload supply. Whether this then translates into a systematic shift to transport capacity being greater than supply for Alpine glaciers will also depend on how glacial melt changes, the latter also declining as glaciers get smaller (Huss & Hock, 2018; Zhang et al., 2022, 2023). If it does, then our results suggest that there should be a progressive decline in the rates of reworking of proglacial braidplains as glaciers retreat. This observation explains the conceptual model of proglacial fluvial morphodynamics following glacier retreat of Gurnell et al. (1999).

Our results emphasize the critical role played by bedload supply in controlling river morphodynamics in this environment. If this declines as glaciers retreat, and capacity can exceed supply, then glacier-supplied sediment may be replaced by reworking of the braid plain, as happened in the second half of 2020. This has to be time-limited. Our data shows how it reduces the spatial extent of reworking whilst the concentration of flow into a set of smaller channels should lead to sediment sorting processes that make it progressively harder to release sediment. This is likely why as deglaciation continues, the sediment yield to downstream declines (Delaney & Adhikari, 2020; Lane et al., 2017; Stoffel & Huggel, 2012) so explaining at least part of the classical model of paraglacial response (Church & Ryder, 1972). In our case, given extreme decoupling of valley side walls from the braidplain by alluvial fans (Mancini & Lane, 2020), it is likely to be the primary explanation.

Further studies are now needed to understand the relationship between the supply to capacity ratio of coarse sediment, proglacial forefield morphodynamics, glacier retreat, and the influence of dead-ice buried within the forefield on sediment transport dynamics, especially to establish robust predictions of sediment supply from glacierized basins in the actual context of rapid climate warming (Zhang et al., 2022). Such changes will also have important implications for the management of downstream sediment transport in hydropower plants (e.g., Carrivick & Tweed, 2021; Li et al., 2021) and for ecosystem stability in high mountain regions (e.g., Gabbud et al., 2019; Miller & Lane, 2019; Roncoroni et al., 2023b). We showed a strong linkage between channel pattern and bedload supply/capacity. Research has also shown that the rates of embryonic ecosystem development in proglacial forefields appear to be very strongly sensitive to fluvial disturbance and access to water (Roncoroni et al., 2023b). If there is a progressive shift to capacity exceeding supply, then reduced disturbance may be countered by reduced access to water due to the development of larger bars (and greater distances to water; Roncoroni et al., 2023b) as well as incised channels and water table draw down (Müller et al., 2024). This is an area that merits further research.

5. Conclusions

In this study, we investigated the geomorphic response of a glacially fed proglacial forefield to deglaciation in two melt seasons experiencing different climatic and glacier-controlled hydrological and sediment supply conditions. The forefield was largely isolated from the valley sidewall sediment supply and contained a braided river. During periods when bedload sediment supply from the glacier exceeds transport capacity there was aggradation, more intense bar construction, increasing channel instability and braiding intensity and coarsening of floodplain deposits. Coarsening was spatially focused on flow divergence regions and bar tops. The forefield was also a sink for both bedload and suspended load sediments. In contrast, when the subglacial bedload export rates were lower than transport capacity, the forefield continued to act as a sediment sink for fine sediment reflected in the fining of

surficial deposits. However, the system was net degradational, reflecting in particular the loss of significant bedload sized sediment. Changes in the balance between glacial sediment supply and transport capacity resulted in rapid (timescale of days) changes in river morphodynamics. In the actual context of rapid climate change, these results have major implications for the prediction of sediment supply from glacierized catchments as the magnitude of forefield connectivity with downstream regions is likely to be driven by the interplay between sediment availability and transport capacity, either related to meltwater discharge or extreme precipitation events. Given recent work concerning the relationship between access to water and bar destruction and the intensity of ecosystem engineering by primary colonizers, it further suggests that this balance may impact ecosystem succession in proglacial forefields following their deglaciation.

Data Availability Statement

The data used in this study (i.e., DEMs, orthomosaics and grain size distribution maps) are available in Mancini et al. (2024b). Other data sets used in this study (i.e., water discharge records, 2020 orthomosaics, suspended load and bedload flux data) are archived in Zenodo and mentioned in the main text as Müller and Miesen (2022), Roncoroni et al. (2023a) and Mancini et al. (2023a).

References

Adams, J. (1979). Gravel size analysis from photographs. *Journal of the Hydraulics Division*, *105*(10), 1247–1255. https://doi.org/10.1061/jyceaj.0005283

Anderson, S. W. (2019). Uncertainty in quantitative analyses of topographic change: Error propagation and the role of thresholding. *Earth Surface Processes and Landforms*, *44*(5), 1015–1033. https://doi.org/10.1002/esp.4551

Antoniazza, G., Bakker, M., & Lane, S. (2019). Revisiting the morphological method in two-dimensions to quantify bed material transport in braided rivers. *Earth Surface Processes and Landforms*, *44*(11), 2251–2267. https://doi.org/10.1002/esp.4633

Antoniazza, G., Nicollier, T., Boss, S., Mettra, F., Badoux, A., Schaefli, B., et al. (2022). Hydrological drivers of bedload transport in an Alpine watershed. *Water Resources Research*, *58*(3), e2021WR030663. https://doi.org/10.1029/2021WR030663

Ashmore, P. (1991a). Channel Morphology and bed load pulses in braided, gravel-bed streams. *Geografiska Annaler - Series A: Physical Geography*, *73*(1), 37–52. https://doi.org/10.2307/521212

Ashmore, P. (1991b). How do gravel-bed rivers braid? *Canadian Journal of Earth Sciences*, *28*(3), 326–341. https://doi.org/10.1139/e91-030

Ashmore, P., Bertoldi, W., & Gardner, J. T. (2011). Active width of gravel-bed braided rivers. *Earth Surface Processes and Landforms*, *36*(1), 1510–1521. https://doi.org/10.1002/esp.2182

Ashmore, P. E. (1982). Laboratory modelling of gravel braided stream morphology. *Earth Surface Processes and Landforms*, *7*(3), 201–225. https://doi.org/10.1002/esp.3290070301

Ashmore, P. E. (1988). Bed load transport in braided gravel-bed stream models. *Earth Surface Processes and Landforms*, *13*(8), 677–695. https://doi.org/10.1002/esp.3290130803

Ashworth, P. J., & Ferguson, R. (1989). Size-selective entrainment of bed load in gravel bed streams. *Water Resources Research*, *25*(4), 627–634. https://doi.org/10.1029/WR025I004P00627

Asselman, N. E. M., & Middelkoop, H. (1995). Floodplain sedimentation: Quantities, patterns and processes. *Earth Surface Processes and Landforms*, *20*(6), 481–499. https://doi.org/10.1002/esp.3290200602

Bertoldi, W., Ashmore, P., & Tubino, M. (2009). A method for estimating the mean bed load flux in braided rivers. *Geomorphology*, *103*(3), 330–340. https://doi.org/10.1016/j.geomorph.2008.06.014

Beylich, A. A., Laute, K., Liermann, S., Hansen, L., Burki, V., Vatne, G., et al. (2009). Subrecent sediment dynamics and sediment budget of the braided Sandur system at Sandane, Erdalen (Nordfjord, Western Norway). *Norsk Geografisk Tidsskrift - Norwegian Journal of Geography*, *63*(2), 123–131. https://doi.org/10.1080/00291950902907934

Bezinge, A., Clark, M. J., Gurnell, A. M., & Warburton, J. (1989). The management of sediment transported by glacial melt-water streams and its significnce for the estimation of sediment yield. *Annals of Glaciology*, *13*, 1–5. https://doi.org/10.1017/s0260305500007527

Brasington, J., Langham, J., & Rumsby, B. (2003). Methodological sensitivity of morphometric estimates of coarse fluvial sediment transport. *Geomorphology*, *53*(3), 299–316. https://doi.org/10.1016/S0169-555X(02)00320-3

Brasington, J., Rumsby, B. T., & McVey, R. A. (2000). Monitoring and modelling morphological change in a braided gravel-bed river using high resolution GPS-based survey. *Earth Surface Processes and Landforms*, *25*(9), 973–990. https://doi.org/10.1002/1096-9837(200008)25:9<973::AID-ESP111>3.0.CO;2-Y

Burtin, A., Cattin, R., Bollinger, L., Vergne, L., Steer, P., Robert, A., et al. (2011). Towards the hydrologic and bed load monitoring from high-frequency seismic noise in a braided river: The "torrent de St Pierre". *French Alps. Journal of Hydrology*, *408*(1–2), 43–53. https://doi.org/10.1016/j.jhydrol.2011.07.014

Butler, J. B., Lane, S. N., & Chandler, J. H. (2001). Automated extraction of grain-size data from gravel surfaces using digital image processing. *Journal of Hydraulic Research*, *39*(5), 519–529. https://doi.org/10.1080/00221686.2001.9628276

Carbonneau, P., Bergeron, N. E., & Lane, S. N. (2005). Automated grain size measurements from airborne remote sensing for long profile measurements of fluvial grain sizes. *Water Resources Research*, *41*(11), W11426. https://doi.org/10.1029/2005WR003994

Carbonneau, P., Lane, S. N., & Bergeron, N. E. (2004). Catchment-scale mapping of surface grain size in gravel bed rivers using airborne digital imagery. *Water Resources Research*, *40*(7), W07202. https://doi.org/10.1029/2009WR002759

Carling, P. A., & Reader, N. A. (1982). Structure, composition and bulk properties of upland stream gravels. *Earth Surface Processes and Landforms*, *7*(4), 349–365. https://doi.org/10.1002/esp.3290070407

Carrivick, J. L., & Heckmann, T. (2017). Short-term geomorphological evolution of proglacial systems. *Geomorphology*, *287*, 3–28. https://doi.org/10.1016/j.geomorph.2017.01.037

Carrivick, J. L., Heckmann, T., Turner, A., & Fischer, M. (2018). An assessment of landform composition and functioning with the first proglacial systems dataset of the central European Alps. *Geomorphology*, *321*, 117–128. https://doi.org/10.1016/j.geomorph.2018.08.030

Carrivick, J. L., & Tweed, F. S. (2021). Deglaciation controls on sediment yield: Towards capturing Spatio-Temporal variability. *Earth-Science Reviews*, *221*, 103809. https://doi.org/10.1016/j.earscirev.2021.103809

Chew, L. C., & Ashmore, P. E. (2001). Channel adjustment and a test of rational regime theory in a Proglacial braided stream. *Geomorphology*, *37*(1), 43–63. https://doi.org/10.1016/S0169-555X(00)00062-3

Church, M., & Ryder, J. (1972). Paraglacial sedimentation: A consideration of fluvial processes conditioned by glaciation. *GSA Bulletin*, *83*(10), 3059–3072. https://doi.org/10.1130/0016-7606(1972)83[3059:PSACOF]2.0.CO;2

Collins, D. N. (2008). Climatic warming, glacier recession and runoff from Alpine basins after the Little Ice Age maximum. *Annals of Glaciology*, *48*, 119–124. https://doi.org/10.3189/172756408784700761

Cook, S. J., Swift, D. A., Kirkbride, M. P., Knight, P. G., & Waller, R. I. (2020). The empirical basis for modelling glacial erosion rates. *Nature Communications*, *11*(1), 759. https://doi.org/10.1038/s41467-020-14583-8

Coulthard, T. J., Lewin, J., & Macklin, M. G. (2005). Modelling differential catchment response to environmental change. *Geomorphology*, *69*(1), 222–241. https://doi.org/10.1016/j.geomorph.2005.01.008

Coulthard, T. J., & Van De Wiel, M. J. (2007). Quantifying fluvial non linearity and finding self-organized criticality? Insights from simulations of river basin evolution. *Geomorphology*, *91*(3), 216–235. https://doi.org/10.1016/j.geomorph.2007.04.011

Cudden, J. R., & Hoey, T. B. (2003). The causes of bedload pulses in a gravel channel: The implications of bedload grain-size distributions. *Earth Surface Processes and Landforms*, *28*(13), 1411–1428. https://doi.org/10.1002/esp.521

Curran, J. H., Loso, M. G., & Williams, H. B. (2017). Glacial conditioning of stream position and flooding in the braid plain of the Exit Glacier foreland, Alaska. *Geomorphology*, *293*, 272–288. https://doi.org/10.1016/j.geomorph.2017.06.004

Davies, T. R. H. (1987). Problems of bed load transport in braided gravel-bed rivers. In C. R. Thorne, J. C. Bathurst, & R. D. Hey (Eds.), *Sediment transport in gravel bed rivers* (pp. 793–811). Chichester: John Wiley & Sons.

Delaney, I., & Adhikari, S. (2020). Increased subglacial sediment discharge in a warming climate: Consideration of ice dynamics, glacial erosion, and fluvial sediment transport. *Geophysical Research Letters*, *47*(7), e2019GL085672. https://doi.org/10.1029/2019GL085672

Dietze, M. (2018). The R package "Eseis" – A software toolbox for environmental seismology. *Earth Surface Dynamics*, *6*(3), 669–686. https://doi.org/10.5194/esurf-6-669-2108

Dietze, M., Lagarde, S., Halfi, E., Laronne, J. B., & Turowski, J. M. (2019). Joint sensing of bedload flux and water depth by seismic data inversion. *Water Surface Research*, *55*(11), 9892–9904. https://doi.org/10.1029/2019WR026072

Egozi, R., & Ashmore, P. (2008). Defining and measuring braiding intensity. *Earth Surface Processes and Landforms*, *33*(14), 2121–2138. https://doi.org/10.1002/esp.1658

Egozi, R., & Ashmore, P. (2009). Experimental analysis of braided channel pattern response to increased discharge. *Journal of Geophysical Research*, *114*(F2), F02012. https://doi.org/10.1029/2008JF001099

Ferguson, R. I., & Ashworth, P. (1992). Spatial patterns of bedload transport and channel change in braided and near braided rivers. In P. Billi, R. D. Hey, C. R. Thorne, & P. Taconni (Eds.), *Dynamics of gravel-bed rivers* (pp. 477–492). John Wiley and Sons.

Fonstad, M. A., Dietrich, J. T., Courville, B. C., Jensen, J. L., & Carbonneau, P. E. (2013). Topographic structure from motion: A new development in photogrammetric measurement. *Earth Surface Processes and Landforms*, *38*(4), 421–430. https://doi.org/10.1002/esp.3366

Frings, R. M., Schütterumpf, H., & Vollmer, S. (2011). Verification of porosity predictors for fluvial sand-gravel deposits. *Water Resources Research*, *47*(7), W07525. https://doi.org/10.1029/2010WR009690

Gabbud, C., Robinson, C. T., & Lane, S. N. (2019). Summer is in winter: Disturbance-driven shifts in macroinvertebrate communities following hydroelectric power exploitation. *Science of the Total Environment*, *650*, 2164–2180. https://doi.org/10.1016/j.scitotenv.2018.09.180

Ganti, V., Lamb, M. P., & McElroy, B. (2014). Quantitative bounds on morphodynamics and implications for reading the sedimentary record. *Nature Communications*, *5*(1), 3298. https://doi.org/10.1038/ncomms4298

Germanoski, D., & Schumm, S. A. (1993). Changes in braided river morphology resulting from aggradation and degradation. *The Journal of Geology*, *101*(4), 451–466. https://doi.org/10.1086/648239

Gimbert, F., Tsai, V. C., Amundson, J. M., Bartholomeus, T. C., & Walter, J. I. (2016). Subseasonal changes observed in subglacial channel pressure, size, and sediment transport. *Geophysical Research Letters*, *43*(8), 3786–3794. https://doi.org/10.1002/2016GL068337

Guillon, H., Mugnier, J.-L., & Buoncristiani, J.-F. (2018). Proglacial sediment dynamics from daily to seasonal scales in a glaciated Alpine catchment (Bossons Glacier, Mont Blanc Massif, France). *Earth Surface Processes and Landforms*, *43*(7), 1478–1495. https://doi.org/10.1002/esp.4333

Gurnell, A. M., Edwards, P. J., Petts, G. E., & Ward, J. V. (1999). A conceptual model for alpine proglacial river channel evolution under changing climatic conditions. *Catena*, *38*(3), 223–242. https://doi.org/10.1016/S0341-8162(99)00069-7

Herman, F., Beyssac, O., Brughelli, M., Lane, S. N., Leprince, S., Adatte, T., et al. (2015). Erosion by an Alpine glacier. *Science*, *350*(6257), 193–195. https://doi.org/10.1126/science.aab2386

Hong, L. B., & Davies, T. R. H. (1979). A study of stream braiding. *GSA Bulletin*, *90*(12_Part_II), 1839–1859. https://doi.org/10.1130/GSAB-P2-90-1839

Howard, A. D., Keetch, M. E., & Vincent, C. L. (1970). Topographical and geomorphic proprieties of braided streams. *Water Resources Research*, *6*(6), 1647–1688. https://doi.org/10.1029/WR006i006p01674

Huss, M., & Hock, R. (2018). Global-scale hydrological response to future glacier mass loss. *Nature Climate Change*, *8*(2), 135–140. https://doi.org/10.1038/s41558-017-0049-x

James, M. R., Antoniazza, G., Robson, S., & Lane, S. N. (2020). Mitigating systematic error in topographic models for geomorphic change detection: Accuracy, precision and considerations beyond off-nadir imagery. *Earth Surface Processes and Landforms*, *45*(10), 2251–2271. https://doi.org/10.1002/esp.4878

Jerolmack, D. J., & Paola, C. (2010). Shredding of environmental signals by sediment transport. *Geophysical Research Letters*, *37*(19), L19401. https://doi.org/10.1029/2010GL044638

Kaser, G., Großhauser, M., & Marzeion, B. (2010). Contribution potential of glaciers to water availability in different climate regimes. *Proceedings of the National Academy of Sciences*, *107*(47), 20223–20227. https://doi.org/10.1073/pnas.1008162107

Kasprak, A., Wheaton, J. M., Ashmore, P. E., Hensleigh, J. W., & Peirce, S. (2015). The relationship between particle travel distance and channel morphology: Results from physical models of braided rivers. *Journal of Geophysical Research: Earth Surface*, *120*(1), 55–74. https://doi.org/10.1002/2014JF003310

Lane, S. N., Bakker, M., Gabbud, C., Micheletti, N., & Saugy, J.-N. (2017). Sediment export, transient landscape response and catchment-scale connectivity following rapid climate warming and Alpine glacier recession. *Geomorphology*, *277*, 210–227. https://doi.org/10.1016/j.geomorph.2016.02.015

Lane, S. N., Gentile, A., & Goldenschue, L. (2020). Combining UAV-based SfM-MVS photogrammetry with conventional monitoring to set environmental flows: Modifying Dam flushing flows to Improve alpine stream habitat. *Remote Sensing*, *12*(23), 3868. https://doi.org/10.3390/rs12233868

Lane, S. N., & Nienow, P. W. (2019). Decadal-scale climate forcing of Alpine glacial hydrological systems. *Water Resources Research*, *55*(3), 2478–2492. https://doi.org/10.1029/2018WR024206

Lane, S. N., Richards, K. S., & Chandler, J. H. (1996). Discharge and sediment supply controls on erosion and deposition in a dynamic alluvial channel. *Geomorphology*, *15*(1), 1–15. https://doi.org/10.1016/0169-555X(95)00113-J

Lane, S. N., Westaway, R. M., & Murray Hicks, D. (2003). Estimation of erosion and deposition volumes in a large, gravel-bed, braided river using synoptic remote sensing. *Earth Surface Processes and Landforms*, *28*(3), 249–271. https://doi.org/10.1002/esp.483

Li, D., Overeem, I., Kettner, A. J., Zhou, Y., & Lu, X. (2021). Air temperature regulates erodible landscape, water, and sediment fluxes in the permafrost-dominated catchment on the Tibetan plateau. *Water Resources Research*, *57*(2), e2020WR028193. https://doi.org/10.1029/2020WR028193

Liesle, T. E., Iseya, F., & Hikeda, H. (1993). Response of a channel with alternate bars to a decrease in supply of mixed-size bed load: A flume experiment. *Water Resources Research*, *29*(11), 3623–3629. https://doi.org/10.1029/93WR01673

Maizels, J. (2002). Sediments and landforms of modern proglacial terrestrial environments. In J. Menzies (Ed.), *Modern and past glacial environments* (pp. 279–316). Elsevier. https://doi.org/10.1116/B978-0-7506-4226-2.X5000-4

Mancini, D., Antoniazza, G., Roncoroni, M., Mettra, F., & Lane, S. N. (2024a). Heuristic estimation of river bathymetry in braided stream using digital image processing. *Earth Surface Processes and Landforms*. https://doi.org/10.1002/esp.5944

Mancini, D., Dietze, M., Jenkin, M., Miesen, F., & Lane, S. N. (2023a). Suspended sediment load and bedload flux from the Glacier d'Otemma proglacial forefield (summers 2020 and 2021) [Dataset]. *Zenodo*. https://doi.org/10.5281/zenodo.8380815

Mancini, D., Dietze, M., Müller, T., Jenkin, M., Miesen, F., Roncoroni, M., et al. (2023b). Filtering of the signal of sediment export from a Glacier by its proglacial forefield. *Geophysical Research Letters*, *50*(21), e2023GL106082. https://doi.org/10.1029/2023GL106082

Mancini, D., & Lane, S. N. (2020). Changes in sediment connectivity following glacial debuttressing in an Alpine valley system. *Geomorphology*, *352*, 106987. https://doi.org/10.1016/j.geomorph.2019.106987

Mancini, D., Roncoroni, M., Miesen, F., Pythoud, Q., & Lane, S. N. (2024b). Temporal morphodynamic evolution of the Glacier d'Otemma proglacial forefield for melt seasons 2020 and 2021: Data collection and posit processing [Dataset]. *Zenodo*. https://doi.org/10.5281/zenodo.11347458

Manger, E. G. (1963). *Porosity and bulk density of sedimentary rocks*. Geological Survey Bulletin 1144-E). U.S. Atomic Energy Commission, United States Government Printing Office.

Marren, P. M. (2002). Glacier margin fluctuations, Skaftafellsjökull, Iceland: Implications for Sandur evolution. *Boreas*, *31*(1), 75–81. https://doi.org/10.1111/j.1502-3885.2002.tb01057.x

Marren, P. M., & Toomath, S. C. (2013). Fluvial adjustments in response to glacier retreat: Skaftafellsjökull, Iceland. *Boreas*, *42*(1), 57–70. https://doi.org/10.1111/j.1502-3885.2012.00275.x

Marren, P. M., & Toomath, S. C. (2014). Channel pattern of Proglacial Rivers: Topographic forcing due to glacier retreat. *Earth Surface Processes and Landforms*, *39*(7), 943–951. https://doi.org/10.1002/esp.3545

Miller, H. R., & Lane, S. N. (2019). Biogeomorphic feedbacks and the ecosystem engineering of recently Deglaciated terrain. *Progress in Physical Geography: Earth and Environment*, *43*(1), 24–45. https://doi.org/10.1177/0309133318816536

Mosley, M. P. (1982). Analysis of the effect of changing discharge on channel morphology and instream uses in a Braided River, Ohau River, New Zealand. *Water Resources Research*, *18*(4), 800–812. https://doi.org/10.1029/WR018i004p00800

Mosley, M. P. (1983). Response of braided rivers to changing discharge. *Journal of Hydrology (New Zealand)*, *22*(1), 18–67.

Müller, T., & Miesen, F. (2022). Stream discharge, stage, electrical conductivity & temperature dataset from Otemma glacier forefield, Switzerland (from July 2019 to October 2021) [Dataset]. *Zenodo*. https://doi.org/10.5281/zenodo.6202732

Müller, T., Roncoroni, M., Mancini, D., Lane, S. N., & Schaefli, B. (2024). Current and future role of meltwater-groundwater dynamics in a proglacial Alpine outwash plain. *Hydrology and Earth System Sciences*, *28*(4), 735–759. https://doi.org/10.5194/hess-28-753-2024

Nicholas, A. P. (2013). Modelling the continuum of river channel patterns. *Earth Surface Processes and Landforms*, *38*(10), 1187–1196. https://doi.org/10.1002/esp.3431

Nicholas, A. P., Ashworth, P. J., Kirkby, M. J., Macklin, M. G., & Murray, T. (1995). Sediment slugs: Large-scale fluctuations in fluvial sediment transport rates and storage volumes. *Progress in Physical Geography: Earth and Environment*, *19*(4), 500–519. https://doi.org/10.1177/030913339501900404

Parker, G. (1979). Hydraulic geometry of active gravel-bed rivers. *Journal of the Hydraulics Division*, *105*(9), 1185–1201. https://doi.org/10.1061/jyceaj.0005275

Perolo, P., Bakker, M., Gabbud, C., Moradi, G., Rennie, C., & Lane, S. N. (2019). Subglacial sediment production and snout marginal ice uplift during the late ablation season of a temperate valley glacier. *Earth Surface Processes and Landforms*, *44*(5), 1117–1136. https://doi.org/10.1002/esp.4562

Rickenmann, D. (2020). Effect of sediment supply on cyclic fluctuations of the disequilibrium ratio and threshold transport discharge, inferred from bedload transport measurements over 27 Years at the Swiss Erlenbach stream. *Water Resources Research*, *56*(11), e2020WR027741. https://doi.org/10.1029/2020WR027741

Riihimaki, C. A., MacGregor, K. R., Anderson, R. S., Anderson, S. P., & Loso, M. G. (2005). Sediment evacuation and glacial erosion rates at a small alpine glacier. *Journal of Geophysical Research (Earth Surface)*, *110*(F3), F03003. https://doi.org/10.1029/2004JF000189

Roncoroni, M., Mancini, D., Kohler, T. J., Miesen, F., Gianini, M., Battin, T. J., & N. Lane, S. (2022). Centimeter-scale mapping of phototrophic biofilms in glacial forefields using visible band ratios and UAV imagery. *International Journal of Remote Sensing*, *43*(13), 4723–4757. https://doi.org/10.1080/01431161.2022.2079963

Roncoroni, M., Mancini, D., & Miesen, F. (2023a). SfM-MVS Derved Orthomosaics of the Otemma glacier forefield (2020) [Dataset]. *Zenodo*. https://doi.org/10.5281/zenodo.7514935

Roncoroni, M., Mancini, D., Miesen, F., Müller, T., Gianini, M., Ouvry, B., et al. (2023b). Decrypting the stream periphyton physical habitat of recently deglaciated floodplains. *Science of the Total Environment*, *867*, 161374. https://doi.org/10.1016/j.scitotenv.2022.161374

Roussel, E., Marren, P. M., Cossart, E., Toumazet, J.-P., Chenet, M., Grancher, D., & Jomelli, V. (2018). Incision and aggradation in Proglacial rivers: Post-Little Ice Age long-profile adjustments of Southern Iceland outwash plains. *Land Degradation & Development*, *29*(10), 3753–3771. https://doi.org/10.1002/ldr.3127

Schneider, J. M., Rickenmann, D., Turowski, J. M., Bunte, K., & Kirchner, J. W. (2015). Applicability of bed load transport models for mixed-size sediments in steep streams considering macro-roughness. *Water Resources Research*, *51*(7), 5260–5283. https://doi.org/10.1002/2014WR016417

Schuurman, F., & Kleinhans, M. G. (2015). Bar dynamics and bifurcation evolution in a modelled braided sand-bed river. *Earth Surface Processes and Landforms*, *40*(10), 1318–1333. https://doi.org/10.1002/esp.3722

Stoffel, M., & Huggel, C. (2012). Effects of climate change on mass movements in mountain environments. *Progress in Physical Geography: Earth and Environment*, *36*(3), 421–439. https://doi.org/10.1177/0309133312441010

Swiss Federal Office of Topography (Swisstopo). (2020). Orthophotomosaic SWISSIMAGE [Dataset]. *Swiss Federal Authorities*. Retrieved from https://www.swisstopo.admin.ch/en/orthoimage-swissimage-10

Tabesh, M., Vollmer, S., Schüttrumpf, H., & Frings, R. M. (2022). Spatial variability in river bed porosity determined by nuclear density gauging: A case study from a French gravel-bed river. *Sedimentology*, *62*(2), 823–844. https://doi.org/10.1111/sed.12928

Warburton, J. (1996). Active Braidplain width, bed load transport and channel morphology in a model braided river. *Journal of Hydrology New Zealand*, *35*, 259–285.

Westaway, R. M., Lane, S. N., & Hicks, D. M. (2003). Remote survey or large-scale braided, gravel-bed rivers using digital photogrammetry and image analysis. *International Journal of Remote Sensing*, *24*(4), 795–815. https://doi.org/10.1080/01431160110113070

Wilcock, P. R., & Crowe, J. C. (2003). Surface-based transport model for mixed-size sediment. *Journal of Hydraulic Engineering*, *129*(2), 120–128. https://doi.org/10.1061/(asce)0733-9429(2003)129:2(120)

Wilcock, P. R., Pitlick, J., & Cui, Y. (2009). *Sediment transport primer: Estimating bed-material transport in gravel-bed Rivers*. U.S. Department of Agriculture, Forest Service, General Technical Report RMRS-GTR-226.

Williams, R., Brasington, J., Vericat, D., Hicks, M., Labrosse, F., & Neal, M. (2011). Monitoring braided river change using terrestrial laser scanning and optical bathymetric mapping. In M. J. Smith, P. Paron, & J. S. Griffiths (Eds.), *Developments in Earth surface processes* (Vol. 15, pp. 507–532). Elsevier. https://doi.org/10.1016/B978-0-444-53446-0.00020-3

Williams, R. D., Measures, R., Hicks, D. M., & Brasington, J. (2016). Assessment of a numerical model to reproduce event-scale erosion and deposition distributions in a braided river. *Water Resources Research*, *52*(8), 6621–6642. https://doi.org/10.1002/2015WR018491

Wolman, M. G. (1954). A method of sampling Coarse River-bed material. *Eos, Transactions American Geophysical Union*, *35*(6), 951–956. https://doi.org/10.1029/TR035i006p00951

Zhang, T., Li, D., East, A. E., Kettner, A. J., Best, J., Ni, J., & Lu, X. (2023). Shifted sediment-transport regimes by climate change and amplified hydrological variability in cryosphere-fed rivers. *Science Advances*, *9*(45), eadi5019. https://doi.org/10.1126/sciadv.adi5019

Zhang, T., Li, D., East, A. E., Walling, D. E., Lane, S., Overeem, I., et al. (2022). Warming-driven erosion and sediment transport in cold regions. *Nature Reviews Earth & Environment*, *3*(12), 832–851. https://doi.org/10.1038/s43017-022-00362-0